

Fundamental Performance of a Dispersed Fixed Delay Interferometer In Searching For Planets Around M Dwarfs

Ji Wang, Jian Ge, Peng Jiang, & Bo Zhao

Department of Astronomy, 211, Bryant Space Science Center, University of Florida, Gainesville, FL, 32611

jwang@astro.ufl.edu

ABSTRACT

We present a new method to calculate fundamental Doppler measurement limits with a dispersed fixed-delay interferometer (DFDI) in the near infrared (NIR) wavelength region for searching for exoplanets around M dwarfs in the coming decade. It is based on calculating the Q factor, a measure of flux-normalized Doppler sensitivity in the fringing spectra created with DFDI. We calculate the Q factor as a function of spectral resolution R , stellar projected rotational velocity $V \sin i$, stellar effective temperature T_{eff} and optical path difference (OPD) of the interferometer. We also compare the DFDI Q factor to that for the popular cross-dispersed echelle spectrograph method (the direct echelle (DE) method). We find that: 1, Q_{DFDI} is a factor of 1.5 to 3 higher than Q_{DE} at R ranging from 5,000 to 20,000; 2, Q_{DFDI} and Q_{DE} converge at a very high R ($R \geq 100,000$); 3, Q_{DFDI} increases as R increases and $V \sin i$ decreases; 4, for a given R , Q_{DFDI} increases as T_{eff} drops from 3100K to 2400K (M4V to M9V). We also investigate how Q_{DFDI} is affected by OPD and find that a 5 mm deviation from the optimal OPD does not significantly affect Q_{DFDI} (10% or less) for a wide range of R . Given the NIR Doppler measurement is likely to be detector-limited for a while, we introduce new merit functions, which is directly related to photon-limited RV uncertainty, to evaluate Doppler performance with the DFDI and DE methods. We find that DFDI has strength in wavelength coverage and multi-object capability over the DE for a limited detector resource. We simulate the performance of the InfraRed Exoplanet Tracker (IRET) based on the DFDI design, being considered for the next generation IR Doppler measurements. The predicted photon-limited RV uncertainty suggests that IRET is capable of detecting Earth-like exoplanets in habitable zone around nearby bright M dwarfs if they exist. A new method is developed to quantitatively estimate the influence of telluric lines on RV uncertainty. Our study shows that photon-limited RV uncertainty can be reached if 99% of the strength of telluric lines can be removed from the measured stellar spectra. At low to moderate levels of telluric line strength removal (50% to 90%), the optimal RV uncertainty is typically a factor of 2-3 times larger than photon-limited RV uncertainty.

Subject headings: planetary systems-techniques: radial velocities

1. Introduction

There are over 500 detected exoplanets as of June 2011 and about 80% of them were first discovered by the radial velocity (RV) technique using ground-based Doppler instruments¹. The popular Doppler instruments are based on the cross-dispersed echelle spectrograph design, which we called the direct echelle (DE) method. In this method, the RV signals are extracted by directly measuring the centroid shift of stellar absorption lines. The fundamental photon-limited RV uncertainty using the DE method has been studied and reported by several research groups (e.g., Butler et al. (1996); Bouchy et al. (2001)). The best achieved RV precision with the DE instrument is less than $1 \text{ m} \cdot \text{s}^{-1}$ RV precision with bright and stable stars using the High Accuracy Radial Velocity Planet Searcher (HARPS) on the European Southern Observatory 3.6 meter telescope (Bouchy et al. 2009). While DE is the most widely adopted method in precision RV measurements, a totally different RV method using a dispersed fixed delay interferometer (DFDI) has also demonstrated its capability in discovering exoplanets (Ge et al. 2006; Fleming et al. 2010; Lee et al. 2011). In this method, the RV signals are derived from phase shift of the interference fringes created by passing stellar absorption spectra through a Michelson type interferometer with fixed optical path difference (OPD) between the two interferometer arms (Erskine & Ge 2000; Ge 2002a,b; Erskine 2003). The stellar fringes are separated by a post-disperser, which is typically a medium-resolution spectrograph. Doppler sensitivity of DFDI can be optimized by carefully choosing the optical path difference of the interferometer. The DFDI method is promising for its low cost, compact size and potential for multi-object capability (Ge 2002b). van Eyken et al. (2010) discussed the theory and application of DFDI in detail. However, its fundamental limit for Doppler measurements has not been well studied before. In this paper, we introduce a method to calculate photon-noise limited Doppler measurement uncertainty in the near infrared (NIR) wavelength region, where we plan to apply the DFDI method for launching a Doppler planet survey around M dwarfs.

IR Doppler planet surveys are very important to address planet characteristics around low mass stars, especially M dwarfs. M dwarfs emit most of their photons in the NIR region. Due to lack of NIR Doppler techniques, only a few hundreds of the brightest M dwarfs have been searched for exoplanets using optical DE instruments (Wright et al. 2004; Endl et al. 2006; Zechmeister et al. 2009; Blake et al. 2010). To date, only about 20 exoplanets around M dwarfs have been discovered compared to more than 500 exoplanets discovered around solar type stars (i.e., FGK stars) despite of the fact that M dwarfs account for 70% stars in local universe. Nonetheless, searching for planets around M dwarfs is essential to answer questions such as the dependence of planetary properties on the spectral type of host stars. In addition, the smaller stellar mass of M dwarfs favors detection of rocky planets in habitable zone (HZ) using the RV technique. However, the stellar absorption lines in NIR are not as sharp as those in the visible band. Recent study by Reiners et al. (2010) shows that precision RV measurements can only reach better Doppler precision in the NIR than in

¹<http://exoplanet.eu/>; <http://exoplanets.org/>

visible wavelength for M dwarfs with stellar types later than M4. In this paper, we report results from our study on fundamental limits with the NIR Doppler technique using the DFDI method.

This paper is organized as follows. In §2, we briefly review the principle of DFDI. In §3, we describe the methodology of simulations in which we compute photon-limited RV uncertainty for both DE and DFDI. In §4, we compare the RV uncertainties of DE and DFDI under various conditions. In §5, we predict the photon-limited performance of a DFDI-based Doppler instrument in the NIR and discuss its potential contributions to exoplanets search around M dwarfs. In §6, we discuss the influence of telluric lines on precision RV measurements and different methods of removing telluric line effects. A summary of the study is given in §7.

2. Brief Review of DFDI

The theory of DFDI has been discussed by several papers (Ge 2002b; Erskine 2003; van Eyken et al. 2010). We briefly introduce the principle of DFDI in this section, readers may refer to previous references for more detailed discussion. DFDI is realized by coupling a fixed delay interferometer with a post-disperser (Fig. 1). The resulting fringing spectrum is recorded on a 2-D detector. The formation of the final fringing spectrum is illustrated in Fig. 2. $B(\nu, y)$ is a mathematical representation of the final image formed at the 2-D detector and it is described by the following equation:

$$B(\nu, y) = \left[\frac{S_0(\nu)}{h\nu} \times IT(\nu, y) \right] \otimes LSF(\nu, R), \quad (1)$$

where $S_0(\nu)$ is the intrinsic stellar spectrum and ν is optical frequency. S_0 is divided by $h\nu$ to convert energy flux into photon flux. IT is the intensity transmission function (Equation (2)), y is the coordinate along the slit direction which is transverse to dispersion direction, \otimes represents convolution and LSF is the line spread function of the post-disperser which is a function of ν and spectral resolution R . In Equation (2): γ is visibility for a given frequency channel, the ratio of half of the peak-valley amplitude and the DC offset, which is determined by stellar flux $S_0(\nu)$; c is the speed of light; and τ is the optical path difference (OPD) of the interferometer which is designed to be tilted along the slit direction such that several fringes are formed along each ν channel (Middle, Fig. 2). We assume the LSF is a gaussian function (Equation (3)), $\Delta\nu = \nu/R/2.35$ because we assume that one resolution element is equal to the FWHM of a spectral line.

$$IT = 1 + \gamma(\nu) \cdot \cos \left(\frac{2\pi\nu\tau(\nu, y)}{c} \right), \quad (2)$$

$$LSF(\nu_0, \Delta\nu) = \frac{1}{2\pi\nu^2} \exp \left(- \frac{(\nu - \nu_0)^2}{2\Delta\nu^2} \right). \quad (3)$$

Fig. 3 shows high-resolution (0.005 Å spacing) synthetic spectra of M dwarfs with solar metallicity (Hauschildt et al. 1999; Allard et al. 2001). T_{eff} ranges from 2400K to 3100K, and $\log g$ is 4.5. No rotational broadening is added in the spectrum. Most absorption lines are shallow

with FWHMs of several tenths of an Å. Since RV information is embedded in the slope of an absorption line, sharp and deep lines contain more RV information than broad and shallow lines. Mathematically, the slope is the derivative of flux as a function of optical frequency, i.e., $dS_0/d\nu$. The power spectrum of $dS_0/d\nu$ is obtained by Fourier transform. According to properties of Fourier transform, $\mathcal{F}[dS_0/d\nu] = (i\rho) \cdot \mathcal{F}[S_0]$, where \mathcal{F} manifests Fourier transform, i is the unit of imaginary number and ρ is the representation of ν/c in Fourier space. We plot $\mathcal{F}([dS_0/d\nu])$ in Fig. 4 as well as the spectral response function (SRF), which is $\mathcal{F}[LSF]$. SRF at $R = 5,000$ drops drastically toward high spatial frequency (high ρ value) such that it misses most of the RV information contained in stellar spectrum. As R increases, SRF gradually increases toward high ρ where the bulk of RV information is stored. A spectrograph with R of $\sim 100,000$ is capable of nearly completely extracting RV information. Unlike DE, DFDI can shift $\mathcal{F}[dS_0/d\nu]$ by an amount determined by the OPD of the interferometer (Erskine 2003). For example, Fig. 4 also shows the power spectrum of $\mathcal{F}([dS_0/d\nu])$ of a fringing spectrum obtained with a DFDI instrument with a 20 mm optical delay, which shifts $\mathcal{F}[dS_0/\nu]$ by 20 mm. In this case, RV information has been shifted from the original high spatial frequencies to low spatial frequencies which can be resolved by a spectrograph with a low or medium R in DFDI.

3. Simulation Methodology

In the DE method, an efficient way based on a spectral quality factor (Q) was introduced by Bouchy et al. (2001) to calculate the fundamental uncertainty in the Doppler measurements. The Q factor is a measure of spectral profile information within a given wavelength region considered for Doppler measurements. Here we develop a similar method to calculate Q values for the DFDI method. Instead of representing the spectral line profile information in the DE method, the Q factor in our DFDI method represents stellar fringe profile information. We use high resolution (0.005 Å spacing) synthetic stellar spectra generated by PHOENIX code (Hauschildt et al. 1999; Allard et al. 2001) because observed spectra of low mass stars do not have high enough resolution and broad effective temperature coverage. Reiners et al. (2010) have conducted several comparisons between synthetic spectra generated by PHOENIX and the observed spectra. They concluded that the synthetic spectra are accurate enough for RV measurement uncertainty calculation. We used synthetic stellar spectra of solar abundance with T_{eff} ranging from 2400K to 3100K (corresponding spectral type from M9V to M4V) and a surface gravity $\log g$ of 4.5. The Q factor is calculated for a series of 10 nm spectral slices from 800 nm to 1350 nm. We artificially broaden spectra with $V \sin i$ from 0 $\text{km} \cdot \text{s}^{-1}$ to 10 $\text{km} \cdot \text{s}^{-1}$ assuming a limb darkening index of 0.6, which is a typical value for an M dwarf. We convolve the rotational broadening profile with each spectral slice of 10 nm to obtain a rotationally-broadened spectrum. We assume a Gaussian LSF which is determined by spectral resolution R (Equation (3)). After artificial rotational broadening and LSF convolution, we rebin each spectral slice according to 4.2 pixels per resolution element (according to the optical design of IRET by Zhao et al. (2010)) to generate the final 2D image on a detector based on which we compute the Q factor.

3.1. Photon-limited RV Uncertainty of DE

Bouchy et al. (2001) described a method of calculating the Q factor for the DE method. We briefly introduce the method here and the reader can refer to Bouchy et al. (2001) for more details. Let $S_0(\nu)$ designate an intrinsic stellar spectrum. A_0 , a digitalized and calibrated spectrum, is considered as a noise-free template spectrum for differential RV measurement, which is related to $S_0(\nu)$ via the following equation:

$$A_0(i) = \frac{S_0(\nu)}{h\nu} \otimes LSF(\nu), \quad (4)$$

where i is pixel number and S_0 is divided by $h\nu$ to convert energy flux into photon flux. Another spectrum A is taken at a different time with a tiny Doppler shift, which is small relative to the typical line width of an intrinsic stellar absorption. Assuming that the two spectra have the same continuum level, Doppler shift is given by:

$$\frac{\delta v}{c} = \frac{\delta \nu}{\nu}, \quad (5)$$

where c is speed of light and ν is optical frequency. The overall RV uncertainty for the entire spectral range is given by (Bouchy et al. 2001):

$$\frac{\delta v_{rms}}{c} = Q^{-1} \cdot \left[\sum_i A_0(i) \right]^{-1/2} = \frac{1}{Q\sqrt{N_{e-}}}, \quad (6)$$

where Q is defined as:

$$Q \equiv \left[\frac{\sum_i W(i)}{\sum_i A_0(i)} \right]^{1/2}, \quad (7)$$

and $W(i)$ is expressed as:

$$W(i) = \frac{\left(\frac{\partial A_0(i)}{\partial \nu(i)} \right)^2 \nu(i)^2}{A(i)}. \quad (8)$$

The Q factor is independent of photon flux and represents extractable Doppler information given an intrinsic stellar spectrum and instrument spectral resolution R . According to Equation (6), we can calculate photon-limited RV uncertainty given the Q factor and photon flux $N_{e-} = \sum_i A_0(i)$ within the spectral range.

3.2. Photon-limited RV Uncertainty of DFDI

A new method of calculating the Q factor for DFDI is developed and discussed here. After a digitalization process, a 2-D flux distribution expressed by Equation (1) is recorded on a 2-D detector in DFDI. The digitalization process involves distributing photon flux into each pixel

according to: 1) pixels per resolution element (RE); 2) spectral resolution; 3) number of fringes along slit. $B_0(i, j)$, which is a noise-free template, is then calculated. $B(i, j)$ is a frame taken at a different time with a tiny Doppler shift. i is the pixel number along the dispersion direction, and j is the pixel number along the slit direction. The observable intensity change at a given pixel (i, j) in DFDI is expressed by:

$$\begin{aligned} B(i, j) - B_0(i, j) &= \frac{\partial B_0(i, j)}{\partial \nu(i)} \delta \nu(i) \\ &= \frac{\partial B_0(i, j)}{\partial \nu(i)} \cdot \frac{\delta v}{c} \cdot \nu(i). \end{aligned} \quad (9)$$

The Doppler shift is measured by monitoring the intensity change at a given pixel in the equation:

$$\frac{\delta v}{c} = \frac{B(i, j) - B_0(i, j)}{\frac{\partial B_0(i, j)}{\partial \nu(i)} \cdot \nu(i)}. \quad (10)$$

Frame B_0 is assumed to be a noise-free template and the noise of frame B is the quadratic sum of the photon noise and the detector noise σ_D :

$$B_{rms}(i, j) = \sqrt{B(i, j) + \sigma_D^2}. \quad (11)$$

Equation (11) is approximated under photon-limited conditions as $B_{rms}(i, j) = \sqrt{B(i, j)}$. Therefore, the RV uncertainty at pixel (i, j) is given by:

$$\frac{\delta v_{rms}(i, j)}{c} = \frac{\sqrt{B(i, j)}}{\frac{\partial B_0(i, j)}{\partial \nu(i)} \cdot \nu(i)}. \quad (12)$$

The overall RV uncertainty for the entire spectral range is given by:

$$\begin{aligned} \frac{\delta v_{rms}}{c} &= \left[\sum_{i,j} \left(\frac{\delta v_{rms}(i, j)}{c} \right)^{-2} \right]^{-1/2} \\ &\equiv \left[\sum_{i,j} W(i, j) \right]^{-1/2} \\ &\equiv Q^{-1} \cdot \left[\sum_{i,j} B_0(i, j) \right]^{-1/2} \\ &= \frac{1}{Q \sqrt{N_{e^-}}}, \end{aligned} \quad (13)$$

where

$$W(i, j) \equiv \frac{\left(\frac{\partial B_0(i, j)}{\partial \nu(i)} \right)^2 \nu(i)^2}{B(i, j)}, \quad (14)$$

and

$$Q \equiv \left[\frac{\sum_{i,j} W(i,j)}{\sum_{i,j} B_0(i,j)} \right]^{1/2}. \quad (15)$$

Equation (15) calculates the Q factor for the DFDI method, which is also independent of flux and represents the Doppler information that can be extracted with the DFDI method. According to Equation (13), we can calculate photon-limited RV uncertainty given the Q factor and photon flux $N_{e-} = \sum_{i,j} B_0(i,j)$ within the spectral range.

4. Comparison between DE and Optimized DFDI

4.1. Optimized DFDI

Optical Path Difference (OPD) of a fixed delay interferometer is a crucial parameter that affects the Doppler sensitivity of a DFDI instrument (Ge 2002). An optimized OPD can help increase the instrument Doppler sensitivity. We calculate the optimal OPD for spectra of various T_{eff} and $V \sin i$ at different spectral resolutions (Table 1). We assume a wavelength range from 800 nm to 1350 nm and an OPD range from 10mm to 41mm with a step size of 1mm in the calculation as described in §3.2. Optimal OPD is selected as the one which results in the highest Q factor value. Increasing $V \sin i$ or decreasing R naturally broadens absorption lines, decreasing the coherence length of each stellar absorption line (Ge 2002). Consequently, our simulations show in general that the optimal OPD decreases with increasing $V \sin i$ or decreasing R values (Fig. 5). We also note that T_{eff} influence on optimal OPD is not significant.

We investigate how the Q factor is affected if OPD is deviated from the optimal value. We calculate the Q factor when the actual OPD is deviated from the optimal OPD by 5mm. We choose the lower value of the two Q s from the 5 mm deviation from the optimal delay (both positive and negative sides) as Q_{deviated} . We plot the ratio of Q_{optimal} and Q_{deviated} as a function of spectral resolution R in Fig. 6. We found that deviating OPD by 5mm does not result in severe degradation of the Q factor. The maximum degradation is 1.115 and occurs at R of 5,000 and $V \sin i$ of $5 \text{ km} \cdot \text{s}^{-1}$ for a star with T_{eff} of 2800 K. The degradation can be compensated by increasing the integration time by 24% (1.115^2) to reach the same photon-limited Doppler precision according to equation (13). The degradation becomes smaller as R increases. As shown in Fig. 4, DFDI shifts the power spectrum of $dS_0/d\nu$ by an amount determined by the interferometer OPD so that the SRF has a reasonable response at a region where most of the RV information is contained. The SRF broadens as R increases. Therefore, it can still recover most of the RV information in a stellar spectrum even if OPD is deviated from the optimal value. At low and medium resolutions (5,000 to 20,000), Q factor degradation becomes larger as $V \sin i$ increases. This is because rotational broadening removes the high frequency signal from a stellar spectrum, which makes the region containing most

of the RV information more sensitive to the choice of OPD as the power spectrum distribution becomes narrower due loss of high ρ component.

4.2. Influence of Spectral Resolution R

In theory, a spectrograph with an infinitely high resolution would be able to extract all the RV information contained in a stellar spectrum. However, in practice, it is impossible to completely recover the RV information with a spectrograph with a finite spectral resolution whose spectral response function drops at the high spatial frequency end. Although the power spectrum of the derivative of the stellar spectrum is shifted to the low frequency region where most of the RV information is carried, the power spectrum is still broad in the spatial frequency (ρ) domain (see Fig. 4). Thus, high R can help to extract more RV information. In a wavelength coverage from 800 nm to 1350 nm, we calculate Q values for stellar spectra with $V \sin i$ of 0, 2, 5 and 10 $\text{km} \cdot \text{s}^{-1}$ at different R (5,000 to 150,000 with a step of 5,000) in order to investigate the dependence of Q on R (Fig. 7). We find that more RV information (higher Q factor) can be extracted as R increases. Q factors for DFDI and DE converge at high R because the spectral response function is wide enough in the ρ domain to cover the region rich in RV information, not affected by the power spectrum shifting involved in DFDI. In addition, the Q factor at a given R increases as T_{eff} drops from 3100K to 2400K, which is largely due to stronger molecular absorption features in the I, Y and J bands (see Fig. 3).

We divide R into three regions, low resolution (5,000 to 20,000), medium resolution (20,000 to 50,000) and high resolution (50,000 to 150,000). We use a power law to fit Q for both DFDI and DE as a function of R . The power indices χ of three regions for $T_{\text{eff}} = 2400\text{K}$ are presented in Table 2. At low R region, χ remains roughly a constant for $0 \text{ km} \cdot \text{s}^{-1} \leq V \sin i \leq 5 \text{ km} \cdot \text{s}^{-1}$, but it drops for stars with $V \sin i$ of $10 \text{ km} \cdot \text{s}^{-1}$ indicating stellar absorption lines begin to be resolved even at low R . At higher R regions, χ decreases as $V \sin i$ increases, a reduced value of χ implies diminishing benefit brought by increasing R . Stellar absorption lines are broadened by stellar rotation, and they are resolved at a certain R beyond which increasing R does not significantly gain Doppler sensitivity. Overall, χ for DE is larger than that of DFDI, especially for low and medium R . In other words, Q_{DFDI} is less sensitive to a change of R , and the DFDI instrument can extract relatively more Doppler information at low or medium spectral resolution than the DE method. For example, for slow rotators ($V \sin i = 2 \text{ km} \cdot \text{s}^{-1}$) at the low R region ($R = 5,000\text{-}20,000$), $Q_{\text{DFDI}} \propto R^{0.63}$. Doppler sensitivity δv_{rms} is inversely proportional to two factors: Q and $\sqrt{N_{e-}}$ according to Equation (6) and (13), where N_{e-} is the total photon count collected by the CCD detector. $N_{e-} \propto (S/N)^2 \cdot N_{\text{pixel}}$, where S/N is the average signal to noise ratio per pixel, and N_{pixel} is total number of pixels. Note that $N_{e-} \propto R$ if the wavelength coverage, S/N per pixel and the resolution sampling are fixed. Therefore, $\delta v_{rms} \propto R^{-0.63-0.5} = R^{-1.13}$ for DFDI. In comparison, $\delta v_{rms} \propto R^{-1.57}$ for DE given the same wavelength coverage and S/N per pixel. The power law is consistent with the previous theoretical work by Ge (2002b) and Erskine (2003).

We compare Q factors for both DFDI and DE at given R values, and the results are shown in Fig. 8. For very slow rotators ($0 \text{ km} \cdot \text{s}^{-1} \leq V \sin i \leq 2 \text{ km} \cdot \text{s}^{-1}$), the advantage of DFDI over DE is obvious at low and medium R (5,000 to 20,000) because the center of the power spectrum of the derivative of the stellar spectrum is at a high frequency domain which cannot be covered in DE due to the limited frequency response range of its SRF at low and medium R . The improvement of DFDI is ~ 3.1 times ($R=5,000$), ~ 2.4 times ($R=10,000$) and ~ 1.7 times ($R=20,000$) respectively. In other words, optimized DFDI with R of 5,000, 10,000 and 20,000 is equivalent to DE with R of 16,000, 24,000 and 34,000 respectively in terms of Doppler sensitivity for the same wavelength coverage, S/N per pixel and spectral sampling (otherwise, see more discussions in §4.3, the gain with the DFDI would be more significant for a fixed detector size and exposure time). Overall, DE with the same spectral resolution as DFDI at $R=5,000$ -20,000 requires ~ 3 -9 times longer exposure time to reach the same Doppler sensitivity as DFDI if both instruments have the same wavelength coverage and same detection efficiency (i.e., N_{e-} is the same). The improvement of DFDI at $R=20,000$ -50,000 is not as noticeable as at the low R range. The difference between DFDI and DE becomes negligible when R is over 100,000. In other words, the advantage of the DFDI over DE gradually disappears as R reaches high resolution domain ($R > 50,000$). In addition, the improvement for relatively faster rotators ($5 \text{ km} \cdot \text{s}^{-1} \leq V \sin i \leq 10 \text{ km} \cdot \text{s}^{-1}$) with DFDI is less significant than it is for slow rotators.

4.3. Influence of Detector Pixel Numbers

In the NIR, detector pixel number is typically smaller than the optical detector. Furthermore, the total cost for an NIR array is much higher than an optical detector with the same pixel number. In the foreseeable future, detector size may be one of the major limitations for Doppler sensitivity improvement. We study the impact of the limited detector resource on the Doppler measurement sensitivity. Using the same detector resource, we find that it is fair to compare their Doppler performance for the same target with the same exposure to understand strength and weakness for each method although DFDI and DE are totally different Doppler techniques. According to Equation (6) and (13), we define a new merit function,

$$Q' = Q \cdot \sqrt{N_{e-}}, \quad (16)$$

to study photon-limited Doppler performance for both methods with the same detector size. Note that the newly defined merit function is directly related to photon-limited RV uncertainty, i.e., inverse proportionality. N_{e-} is calculated by Equation (17):

$$N_{e-} = \frac{F_* \cdot \eta \cdot S_{\text{tel}} \cdot t_{\text{exp}}}{2.512^{m_J}}, \quad (17)$$

in which F_* is the photon flux in the wavelength coverage region $\Delta\lambda$ of an $m_J = 0$ star with the unit of $\text{photons} \cdot \text{s}^{-1} \cdot \text{cm}^{-2}$; η is instrument total throughput; S_{tel} is the effective surface area of the telescope; t_{exp} is the time of exposure; and m_J is the J band magnitude.

Here we use IRET as an example to illustrate strengths of the DFDI method for Doppler measurements. IRET adopts the DFDI method and has a wavelength coverage from 800 nm to 1350 nm and a spectral resolution of 22,000. For a fixed detector size (i.e., total number of detector pixels) and fixed number of pixels to sample each resolution element, the total wavelength coverage of a Doppler instrument, $\Delta\lambda$, is

$$\Delta\lambda = \frac{N_{\text{pix}}}{P_{\text{order}}} \cdot \frac{\lambda_c}{R \cdot N_S}, \quad (18)$$

where N_{pix} is total number of pixels available on a CCD detector and N_S is the number of pixels per resolution element, λ_c is the central wavelength and P_{order} is the number of pixels sampling each pixel channel between spectral orders². Equation (18) shows that $\Delta\lambda$ is inversely proportional to R . Table 3 gives the relation of R and $\Delta\lambda$ assuming N_{pixel} , P_{order} and N_S as constants. λ_c is set to be 1000 nm because it is approximately the center of the Y band. We calculated the ratio of Q'_{DFDI} and Q'_{DE} in which we use the photon flux of a star with a T_{eff} of 2400K (Fig. 9). Q'_{IRET} is consistently higher than Q'_{DE} regardless of R of the DE instrument. In other words, IRET is able to achieve lower photon-limited RV uncertainty compared to a DE instrument with the same detector. The result seems to be different from the conclusion we drew in §4.2, in which we compare Q factors of the same R and $\Delta\lambda$ and reached a conclusion that DFDI with an R of 22,000 is equivalent to DE with an R of 35,000 (a factor of 1.6 gain) for the same wavelength coverage and the same detection efficiency (Fig. 7). The key difference between this case and the earlier case is the fixed detector resource instead of fixed total collected photon numbers. Since lower spectral resolution allows to cover more wavelengths, more photons will be collected for the same instrument detection efficiency for both DFDI and DEM. Note that Q' consists of two components, Q and N_{e-} . For a given number of pixels on the detector, $N_{e-,\text{DFDI}}$ is higher than $N_{e-,\text{DE}}$ due to the larger wavelength coverage. In addition, $Q_{\text{DFDI}}(\Delta\lambda_{\text{DFDI}})$ is more than $Q_{\text{DE}}(\Delta\lambda_{\text{DE}})$. Consequently, we see in Fig. 9 that Q'_{IRET} is higher than Q'_{DE} at all R of a DE instrument. Fig. 9 also shows that the minimum of $Q'_{\text{DFDI}}/Q'_{\text{DE}}$ is dependent of $V \sin i$. The ratio of Q' reaches a minimum (Q'_{DE} reaches a maximum) around an R of 50,000 for slow rotators ($V \sin i \leq 5 \text{ km} \cdot \text{s}^{-1}$). It increases at the low R end because the spectrograph has not yet resolved stellar absorption lines. On the other hand, the ratio increases at the high R end because of fewer photons (see Table 3). For fast rotators ($V \sin i = 10 \text{ km} \cdot \text{s}^{-1}$), the ratio reaches a minimum around R of 30,000.

For a slow rotator ($V \sin i = 2 \text{ km} \cdot \text{s}^{-1}$) at low R region ($R = 5,000\text{--}20,000$), $Q_{\text{DFDI}} \propto R^{0.63}$. Since Doppler sensitivity δv_{rms} is inversely proportional to two factors: Q and $\sqrt{N_{e-}}$ according to Equation (6) and (13), the Doppler sensitivity becomes nearly independent of spectral resolution for the DFDI method ($\propto R^{-0.13}$) if the detection size (or total number of pixels) is fixed. This indicates that we can use quite moderate resolution spectrograph to disperse the stellar fringes produced by

²In principle, each frequency channel for both DFDI and DE instruments can be designed identical. In practice, the DFDI instrument tends to use ~ 20 pixels to sample fringes in the slit direction, which is only for measurement convenience, not a requirement. In fact, Muirhead et al. (2011) has demonstrated a phase-stepping method which does not require sample fringes in the slit direction.)

the interferometer in a DFDI instrument while maintaining high Doppler sensitivity. This opens a major door for multi-object Doppler measurements using the DFDI method as proposed by Ge (2002). In comparison, the Doppler sensitivity for the DE method still strongly depends on spectral resolution for a fixed number of detector pixels ($\propto R^{-0.57}$), indicating that higher spectral resolution will offer better Doppler sensitivity.

4.4. Influence of Multi-Object Observations

As discussed in §4.2 and 4.3, the DFDI instrument can be designed to have a moderate resolution spectrograph coupled with a Michelson type interferometer. Moderate spectral resolution allows a single order spectrum or a few order spectra to cover a broad wavelength region in the NIR region while keeping the Doppler sensitivity similar to a high resolution DE design which requires a large detector array to cover spectra from a single target. This indicates that the DFDI method has much greater potential for accommodating multiple targets on the same detector as proposed by Ge (2002) than the DE instrument. In order to evaluate the potential impact of multi-object DFDI instruments, we redefine the merit function Q'' as:

$$Q'' = Q \cdot \sqrt{N_{e-}} \cdot N_{obj}^{\alpha}, \quad (19)$$

where N_{obj} is the number of objects that can be monitored simultaneously, and α is the index of importance for multi-object observations. From the perspective of photon count and S/N, multi-object observations are equivalent to an increase of N_{e-} , and thus α is 0.5. However, from an observational efficiency point of view, Q'' should be proportional to N_{obj} because the more objects are observed simultaneously, the quicker the survey is accomplished, and α is therefore equal to 1.

We assume a detector that covers from 800 nm to 1350 nm at $R=100,000$ so that we can use the Q factors obtained in §4.2. N_{e-} is a constant since we assume identical $\Delta\lambda$. N_{obj} is inversely proportional to the number of pixels per object which is proportional to spectral resolution R (Equation (18)). Note that we do not require N_{obj} to be an integer because we can, in principle, fit a fraction of spectrum on a detector to make full use of the detector. Q'' s for both DFDI and DE are calculated. Fig. 10 shows the ratio of Q'' and $Q''_{R=100,000}$ for DFDI under two different assumptions of α . For $\alpha=0.5$, i.e., increase of N_{obj} is equivalent to photon gain, only a slight improvement is achieved if the detector is used for multi-object observations at lower resolution than 100,000. In comparison, from a survey efficiency point of view (i.e., $\alpha=1$), we see a factor of ~ 4 -6 times boost of Q'' in multi-object observations. The truncation at $R=5,000$ is due to a practical reason that a lower resolution than 5,000 is rarely used in planet survey using RV techniques. On the other hand, similar calculation is also conducted for the DE method (Fig. 11), in which we find that high resolution single object observation is an optimal operation mode for DE from a perspective of photon gain ($\alpha=0.5$). At $\alpha=1$, the increase of Q'' is a factor of ~ 3 at the most.

We compare the maximum of Q'' for both DFDI and DE at different $V \sin i$ in Table 4. At $\alpha=0.5$, the advantage of DFDI over DE is ~ 1.1 for a wide range of $V \sin i$. In other words, from the

photon gain point of view, there is no significant difference between DFDI and DE in multi-object RV instruments. However, from the survey efficiency point of view ($\alpha=1$), we see a factor of 3 boost of Q'' in DFDI for slow rotators ($V \sin i \leq 2 \text{ km} \cdot \text{s}^{-1}$), suggesting 9 times faster in terms of survey speed. For fast rotators (i.e., $V \sin i = 10 \text{ km} \cdot \text{s}^{-1}$), the boost drops to 1.78. Our study confirms that the DFDI method has an advantage for multi-object RV measurements over the DE method as suggested by Ge (2002b).

4.5. Influence of Projected Rotational Velocity $V \sin i$

Projected rotational velocity $V \sin i$ broadens stellar absorption lines and thus reduces the Q factor. We carry out simulations calculating Q factors of different $V \sin i$ ($0 \text{ km} \cdot \text{s}^{-1} \leq V \sin i \leq 10 \text{ km} \cdot \text{s}^{-1}$) at $R=150,000$ and various T_{eff} . We assume a wavelength range from 800 nm to 1350 nm. The results are shown in Fig. 12. The Q factor decreases as $V \sin i$ increases. It is clear that slow rotators would be better targets to reach higher photon-limited RV precision because the spectrum of a slow rotator contains more Doppler information.

5. IRET Performance and its Survey Capability

Here we use the IRET as an example to demonstrate the Doppler sensitivity with the DFDI method and its capability for an NIR survey for exoplanets around M dwarfs. IRET has a spectral resolution R of 22,000. It works mainly in the I, Y and J bands from 800 to 1350 nm. 4.2 pixels sample one resolution element and 25 pixels sample the fringes in the slit (y) direction (Zhao et al. 2010).

We conduct a series of simulations as described in §3.2 using synthetic spectra of M dwarfs and the instrument specifications of IRET (Zhao et al. 2010) to seek for an optimized OPD that maximizes the Q factor. Fig. 13 shows results from simulations of M dwarfs at different T_{eff} . It is shown that for T_{eff} ranging from 2400K to 3100K, the Q factor is maximized at an OPD of around 18.0 mm for $V \sin i$ between $3 \text{ km} \cdot \text{s}^{-1}$ and $5 \text{ km} \cdot \text{s}^{-1}$. In addition to the Q factor, we also need photon flux information for a particular star to calculate the photon-limited RV uncertainty (Equation (13)), which is given by Equation (17). We calculate F_* using a synthetic stellar spectrum and then normalize it such that the flux at 1235 nm is $195.2 \text{ photons} \cdot \text{s}^{-1} \cdot \text{\AA}^{-1} \cdot \text{cm}^{-2}$. Instrument throughput is as shown in Fig. 14, which is estimated based on our current optical design (Zhao et al. 2010). Note that the estimation does not consider fiber coupling efficiency, fiber efficiency, seeing coupling loss and atmospheric transmission. We choose the telescope aperture size of 3500 mm as the design reference to calculate S_{tel} . The telescope obscuring structure is accounted for in the total detection efficiency, η . We assume a t_{exp} of 30 min on an $m_J = 9$ star in the RV uncertainty contours. Fig. 15 shows the fundamental photon-limited RV uncertainty for a set of grids of T_{eff} and $V \sin i$. The photon noise limited Doppler precision can reach $\sim 1\text{-}2 \text{ m} \cdot \text{s}^{-1}$ for

slow rotating cool stellar objects. There is a general trend of RV uncertainty increasing from the low T_{eff} and low $V \sin i$ to the high T_{eff} and high $V \sin i$. Average S/N per pixel as a function of wavelength is plotted in Fig. 16.

As of June 2011, there were only six M dwarf exoplanets discovered in the northern hemisphere (Butler et al. 2004; Charbonneau et al. 2009; Forveille et al. 2009; Howard et al. 2010; Haghighipour et al. 2010; Johnson et al. 2010). We compare the velocity semi-amplitude K of these exoplanets and RV uncertainty predicted for IRET (Table 5). All of them would be detectable by IRET under photon-limited conditions. Therefore, IRET is a suitable instrument conducting follow-up RV measurements of these targets to confirm the detection and detect additional planet companions in these systems. We also compare the velocity semi-amplitude, K_{HZ} , of an Earth-mass planet located within the habitable zone (0.05 AU away from the host star) to the IRET photon-noise detection limit and find that the RV uncertainty of IRET is slightly larger than K_{HZ} . It may be challenging to detect a possible Earth-mass planet in the habitable zone of these planet systems. However, IRET is capable of detecting super-Earth exoplanets in the HZ or Earth-like planets in the HZ around nearby brighter M dwarfs under photon-limited condition.

Earlier study showed that NIR RV measurements gain precision for objects later than M4 because of relatively higher flux and increasing stellar absorption features in the NIR (Reiners et al. 2010). In addition, our study in earlier sections showed that stellar rotation intrinsically broadens stellar absorption features and results in less Doppler information, leading to larger RV measurement uncertainty with IRET. Therefore, slow rotating mid-late type M dwarfs would be major science targets for a planet survey with IRET.

We conducted a literature survey to estimate how many potential targets are suitable for the M dwarf survey in the northern sky using IRET. We select our potential survey targets from the LSPM catalog, which was compiled by Lepine (2005) through a photometric survey of the entire northern sky. This catalog is nearly complete for stars with proper motion higher than $0.15''\text{yr}^{-1}$. We apply a color cut, $V-J > 3$, to select M type stars from the LSPM catalog. Table 6 shows the number of M dwarf targets available brighter than certain J band magnitude. However, not all of the bright M dwarfs are suitable targets. In order to reach high precision ($1\text{--}3 \text{ m} \cdot \text{s}^{-1}$), we only choose M dwarfs with $V \sin i$ less than $10 \text{ km} \cdot \text{s}^{-1}$ as major targets. However, previous study shows that there appears to be a trend that the median of $V \sin i$ increases as T_{eff} decreases (Jenkins et al. 2009). According to Jenkins et al. (2009), mid-late type M dwarf $V \sin i$ distribution can be fitted by a power law with an index of -1.12, which indicates that 41% of mid-late M dwarfs have a $V \sin i$ less than $2 \text{ km} \cdot \text{s}^{-1}$ and 74% of them have a $V \sin i$ less than $10 \text{ km} \cdot \text{s}^{-1}$. They also pointed out that 43% of M dwarfs in their sample exhibit an $\text{H}\alpha$ emission that indicates young and active objects not suitable for RV survey. Statistically, there are about 18% of nearby M dwarf targets that are suitable for a precision RV survey (inactive and with $V \sin i < 2 \text{ km} \cdot \text{s}^{-1}$). Based on IRET photon-limited performance, it is likely that IRET can reach less than $3 \text{ m} \cdot \text{s}^{-1}$ photon-limited Doppler precision for over 200 nearby late M dwarfs to detect and characterize Earth-mass and Super-Earth mass planets.

6. Telluric Line Effect

6.1. Quantitative Telluric Line Effect

Ground-based NIR observation is prone to contamination of telluric lines. Precision RV measurements in the NIR is an extreme case that requires significant disentanglement of stellar absorption lines and telluric lines in order to reach photon-limited precision. Even in the Y band (960 to 1080 nm) and J band (1120 to 1320 nm), where telluric line contamination is less severe, there are still many shallow telluric lines (Fig. 17, Lord (1992))¹. Equation (1) should be rewritten as follows if telluric absorption lines are considered:

$$\begin{aligned}
 B(\nu, y) &= \left[\frac{S_0(\nu)}{h\nu} \times AT(\nu) \times IT(\nu, y) \right] \otimes LSF(\nu, R) \\
 &= \left[\frac{S_0(\nu)}{h\nu} \times (1 - AA(\nu)) \times IT(\nu, y) \right] \otimes LSF(\nu, R) \\
 &= \left[\frac{S_0(\nu)}{h\nu} \times IT(\nu, y) \right] \otimes LSF(\nu, R) + \left[-\frac{S_0(\nu)}{h\nu} \times AA(\nu) \times IT(\nu, y) \right] \otimes LSF(\nu, R) \\
 &= B_S(\nu, y) + B_N(\nu, y),
 \end{aligned} \tag{20}$$

where AT is the atmospheric transmission function and AA is the atmospheric absorption function. In Equation (20), photon flux distribution on the detector, B , is comprised of a signal component B_S and a noise component B_N . Ideally, we require that the detector flux change δB is entirely due to the stellar RV change δv_S . However, δB is also partly induced by telluric line shift δv_N resulting from atmospheric behaviors. Therefore, both δv_S and δv_N contribute to δB . We have two sets of RV measurements, $\delta v_S + \sigma(0, \delta v_{rms,S})$ for RV of B_S and $\delta v_N + \sigma(0, \delta v_{rms,N})$ for RV of B_N , where $\sigma(0, \delta)$ represents random numbers following a gaussian distribution with a mean of 0 and a standard deviation of δ . We weight RV measurements with the inverse square of photon-limited RV uncertainties. The final RV measurement is expressed by the following equation:

$$\delta v = \frac{(\delta v_S + \sigma(0, \delta v_{rms,S})) \cdot \delta v_{rms,S}^{-2} + (\delta v_N + \sigma(0, \delta v_{rms,N})) \cdot \delta v_{rms,N}^{-2}}{\delta v_{rms,S}^{-2} + \delta v_{rms,N}^{-2}}. \tag{21}$$

In practical Doppler measurements, δv_S consists two components, stellar RV and Earth's barycentric RV. We assume a constant stellar RV (i.e., no differential stellar RV). The Earth's barycentric motion may be predetermined and the effect is removed from the observed 2-D spectrum by shifting B_S according to the barycentric velocity. Therefore $\delta v_S=0$ for the B_S component. We further assume that B_N has an RV fluctuation of $\sigma(0, \delta v_{N,ATM})$ because of the Earth's turbulent atmosphere. The measured RV uncertainty δv is equal to:

$$\delta v_{rms} = \frac{(\delta v_{rms,S}) \cdot \delta v_{rms,S}^{-2} + (\delta v_{N,ATM}^2 + \delta v_{rms,N}^2)^{1/2} \cdot \delta v_{rms,N}^{-2}}{\delta v_{rms,S}^{-2} + \delta v_{rms,N}^{-2}}, \tag{22}$$

¹<http://atran.sofia.usra.edu/cgi-bin/atran/atran.cgi>

Three examples are considered here to represent different level of telluric contamination to the precision RV measurements: 1, if $\delta v_{rms,S} \gg \delta v_{rms,N}$, then $\delta v_{rms} = (\delta v_{N,ATM}^2 + \delta v_{rms,N}^2)^{1/2}$, and the RV measurement is dominated by atmospheric behaviors, this approximation applies in a wavelength region with dense telluric line distribution; 2, if $\delta v_{rms,S} \ll \delta v_{rms,N}$ (i.e., in very transparent atmosphere windows where few telluric lines exists), then $\delta v_{rms} = \delta v_{rms,S}$, and the RV uncertainty is limited by stellar photon noise; 3, for an intermediate situation, if $\delta v_{rms,S}$ and $\delta v_{rms,N}$ are identical, then we apply the same weight on both RV measurements, $\delta v_{rms} = [\delta v_{rms,S} + (\delta v_{N,ATM}^2 + \delta v_{rms,N}^2)^{1/2}]/2$.

In the practical NIR spectroscopic observations, telluric contamination must be minimized in order to reach high Doppler precision. We investigate the effectiveness of two major ways to remove telluric contamination from the stellar spectra with IRET: telluric line masking and removing, and telluric line modeling and removing. The study results are summarized below.

6.2. Telluric Line Masking

Telluric absorption lines are not homogeneously distributed in the NIR spectra, instead, a large number of telluric lines are from relatively concentrated spectral regions. The simplest way is to mask and remove those severely contaminated regions while leaving the less contaminated stellar lines for RV measurements. This would reduce RV measurement uncertainty caused by telluric line contamination, leading to improved RV precision. However, if too much of the wavelength coverage region is masked and removed, then RV uncertainty due to photon noise would increase. Therefore, a balance between the uncertainty brought by telluric lines contamination and by photon noise must be found and an optimal RV performance can be achieved.

We use an M9 dwarf ($T_{\text{eff}}=2400\text{K}$, $V \sin i=5\text{km} \cdot \text{s}^{-1}$ and $m_J=9$) as an example to illustrate how this masking technique affects the RV measurement precision with IRET. We assume a 30 min exposure time, a wavelength coverage from 800 to 1350 nm and an instrument throughput as shown in Fig. 14. We calculate photon-limited RV uncertainty $\delta v_{S,rms}$ and $\delta v_{N,rms}$ according to Equation (13). We calculate Q factors, Q_S and Q_N , based on the two components, B_S and B_N , in Equation (20). The photon flux of B_S and B_N are calculated from the inputs of the stellar type, magnitude, exposure time, instrument specifications and telluric absorption properties.

In practice, RV uncertainty of B_N is not dominated by photon-noise, instead, it is dominated by atmospheric behaviors such as wind, molecular column density change, etc. Figueira et al. (2010) used HARPS archive data and found that O_2 lines are stable to a $10 \text{ m} \cdot \text{s}^{-1}$ level over 6 years. However, the stability of telluric lines becomes worse if we take into consideration other gas molecules such as H_2O and CO_2 . We assume different levels of RV fluctuation due to atmospheric behaviors $\delta v_{N,ATM}$ ($5 \text{ m} \cdot \text{s}^{-1}$, $10 \text{ m} \cdot \text{s}^{-1}$ and $20 \text{ m} \cdot \text{s}^{-1}$). The uncertainty induced by atmospheric telluric lines is transferred to δv_{rms} via Equation (22) without the effort of disentangling stellar and telluric lines as if the uncertainty is due to photon-noise of B_S . Telluric lines with the largest slope

are masked at the highest priority because they cause the most RV uncertainty in the measurement.

Fig. 18 shows the results of telluric line masking for an M9 dwarf under different levels of telluric line masking. After masking a certain portion of the most severely contaminated stellar spectrum, optimal RV uncertainty v_{rms} is $3.3 \text{ m} \cdot \text{s}^{-1}$, $3.6 \text{ m} \cdot \text{s}^{-1}$ and $3.9 \text{ m} \cdot \text{s}^{-1}$ respectively for $\delta v_{N,ATM}$ of $5 \text{ m} \cdot \text{s}^{-1}$, $10 \text{ m} \cdot \text{s}^{-1}$ and $20 \text{ m} \cdot \text{s}^{-1}$. They are 2.6, 2.8 and 3.0 times worse compared to the fundamental photon-limited RV uncertainty of the stellar spectrum $\delta v_{rms,S}$, i.e., $1.3 \text{ m} \cdot \text{s}^{-1}$. If we do not apply telluric line masking at all, RV uncertainty is dominated by atmospheric behaviors, $\delta v_{N,ATM}$. It is expected that δv_{rms} increases as we mask more of the stellar spectrum because less photon flux is available to calculate RV. Depending on values of $\delta v_{N,ATM}$, the optimal spectrum fraction used in RV measurement lies in between 30% and 50%. Higher value of $\delta v_{N,ATM}$ requires masking and removing larger fraction of stellar spectrum. It is noted that we would have expected δv_{rms} to be only ~ 1.4 times worse than $\delta v_{rms,S}$ after $\sim 50\%$ of the spectrum is masked for pure concern of photon flux. However, δv_{rms} is ~ 3 times worse than $\delta v_{rms,S}$ because not only N_e but also Q is reduced after telluric line masking.

6.3. Telluric Lines Modeling

In principle, the telluric lines can be modeled and removed using a telluric line spectrum template. This kind of template can be obtained by observing fast rotating early type stars since the spectrum of an early type star (early A type in particular) is nearly featureless and a good approximation of a blackbody spectrum in NIR except for broad hydrogen absorption features (Vacca et al. 2003). However, the number of available telluric standard stars limits the application of this method. In addition, the spectrum of a telluric standard star is not entirely featureless, which results in some residuals that undermines precision RV measurements.

As a first order estimation, we consider the simplest case in which we assume that the spectrum of a telluric standard star is a perfect blackbody spectrum with no spectral features which may otherwise be perfectly modeled and removed. Since the spectrum of a science target and the spectrum of a telluric line standard star are not taken simultaneously, the telluric lines' centroids and depths may change over time. We assume that the centroids of telluric lines remain unshifted. As a result, the only uncertainty is the depth of a telluric line. Equation (13) and (20) offer insight in understanding the process of telluric line modeling. In the telluric line modeling, we model the telluric lines by observing a standard star or by forward modeling using a list of telluric lines. We remove telluric lines from the observed spectrum of a science target. The depths of the telluric lines are consequently reduced by a certain fraction depending upon the level of removal, which effectively reduces AA (Atmosphere Absorption). A reduced AA means less photon contribution in B_N and thus less uncertainty induced by atmospheric behaviors.

Fig. 19 shows how RV uncertainty δv_{rms} is correlated with different levels of telluric line modeling and removing. We assume $\delta v_{N,ATM}$ to be $10 \text{ m} \cdot \text{s}^{-1}$. Fig. 20 shows the optimal RV

uncertainty at different removal levels. If no removal is involved, the optimal δv_{rms} is 3 times worse than $\delta v_{rms,S}$. At low levels of telluric line removal, i.e., a small fraction of the strength of telluric lines is removed, it requires to mask out about 30% to 50% of the stellar spectrum to reach an optimal RV uncertainty. As the removal becomes more effective, the influence caused by telluric lines decreases, and only a small portion of the spectrum requires masking. Therefore, the optimal RV uncertainty, δv_{rms} , reaches a smaller value. At a very high level of removal, in which 99% of the strength of telluric lines can be modeled and removed, i.e., the residual of telluric line modeling is only 1%, telluric line masking is not necessary. The entire wavelength coverage region can be used in the RV calculation. δv_{rms} approaches the fundamental photon-limited RV uncertainty, $\delta v_{rms,S}$. In previous study, the residual of telluric lines has reached an rms of 0.7% using a 3-component (absorption gas, telluric lines and star) spectrum to model the observed stellar spectrum (Bean et al. 2010). Therefore, it is quite possible to reach photon noise limited RV precision with IRET using this telluric line modeling and removing method.

7. Summary and Discussion

7.1. Q Factors for DFDI, DE and FTS

We develop a new method of calculating photon-limited Doppler sensitivity of an instrument adopting the DFDI method. We conduct a series of simulations based on high resolution synthetic stellar spectra generated by PHOENIX code (Hauschildt et al. 1999; Allard et al. 2001). In simulations, we investigate the correlations of Q and other parameters such as OPD of the interferometer, spectral resolution R and stellar projected rotational velocity $V \sin i$. We find that optimal OPD increases with increasing R and decreasing $V \sin i$. Empirically, the optimal OPD is chosen such that the density of the interference combs matches with the line density of the stellar spectrum. Based on the simulation results, the optimal OPD is determined as the one that maximizes the Q factor. In fact, optimal OPDs found from empirical way and from numerical simulation are consistent with each other. For example, for $V \sin i = 0 \text{ km} \cdot \text{s}^{-1}$ and $R = 50,000$, simulation gives an optimal OPD of 30 mm. The interference comb density of an interferometer with OPD of 30 mm is $\sim 0.3 \text{ \AA}$ at 1000 nm, which indeed matches the width of a typical absorption line after spectral blurring with R of 50,000. An independent method to calculate photon-noise limited Doppler measurement uncertainty in the optical is being developed, and the results will be reported in a separate paper (Jiang et al. 2011). We have compared results from both methods and confirmed that both independent methods produce essentially the same results for both optical and NIR Doppler measurements.

We investigate how the Q factor is affected if OPD is deviated from the optimal value and find that a deviated OPD (5mm) does not result in a significant Q factor degradation, which is mitigated as R increases. We find that the Q factor increases with R for both DFDI and DE, and eventually converge at very high R ($R \geq 100,000$). The convergence of DFDI and DE methods is a

natural consequence because the measurement method does not make a difference after the spectral resolution becomes extremely high. In addition, Q factors at a given R increase as T_{eff} drops from 3100K to 2400K, which is due to stronger molecular absorption features in NIR (see Fig. 3). The Q factor decreases as $V \sin i$ increases because stellar rotation broadens the absorption lines, leading to less sensitive measurement.

We compare Q factors for both DFDI and DE at a given R . For slow rotators ($0 \text{ km} \cdot \text{s}^{-1} \leq V \sin i \leq 2 \text{ km} \cdot \text{s}^{-1}$), DFDI is more advantageous over DE at low and medium R (5,000 to 20,000) for the same wavelength coverage $\Delta\lambda$. The improvement of DFDI compared to DE is ~ 3.1 ($R=5,000$), ~ 2.4 ($R=10,000$) and ~ 1.7 ($R=20,000$), respectively. In other words, optimized DFDI with R of 5,000, 10,000 and 20,000 are equivalent in Doppler sensitivity to DE with R of 16,000, 24,000 and 34,000, respectively. The improvement of DFDI at R 20,000 to 50,000 is not as noticeable as at low R range. The difference between DFDI and DE becomes negligible when R is over 100,000. For relatively faster rotators ($5 \text{ km} \cdot \text{s}^{-1} \leq V \sin i \leq 10 \text{ km} \cdot \text{s}^{-1}$), the improvement with DFDI is less obvious than it is for very slow rotators. DFDI has strength when the spectral lines in a stellar spectrum are not resolved by a spectrograph, which is the case for low and medium resolution spectrograph. Under such conditions, the fixed delay interferometer provides additional resolving powers for the system. After the lines are fully resolved by the spectrograph itself, the interferometer in the system becomes dispensable, which is the reason why we see the convergence of DFDI and DE at very high spectral resolution.

Fundamental performance of a Fourier-transform spectrometer (FTS) in the application of Doppler measurements has been discussed by Maillard (1996). There are similarities between the FTS and the DFDI method, for example: 1, both methods use the interferometer as a fine spectral resolving element; 2, RV is measured by monitoring the temporal phase change at a fixed OPD of the interferometer. In DFDI method, OPD is scanned in each frequency channel because of two relatively tilted mirrors, and the resolution of the post-disperser in DFDI is chosen to ensure a reasonable fringe visibility. Therefore, the DFDI method is an extended version of the FTS method with a low-medium resolution post-disperser. However, one major difference between these two methods is that the interferometer itself is used as a spectrometer by OPD scanning in the FTS method while an additional spectrograph is employed in the DFDI method. The advantage of introducing an additional spectrograph into the system is that the visibility (or fringe contrast) is no longer limited by the bandpass as in the FTS case, which is the reason that the DFDI method can be applied in broad-band Doppler measurements. Mosser et al. (2003) discussed the possibility of an FTS working in broad band by introducing a low resolution post-disperser and concluded that the FTS method is inferior (by a factor between 1 and 2) to DE method even after employing an post-disperser. This conclusion should be accepted with cautions because they compared an FTS with a post-disperser ($R=1200$) with a DE instrument with a much higher spectral resolution ($R=84,000$), which is not necessarily a fair comparison.

We define new merit functions (Equations (16) and (19)) to objectively evaluate Doppler performance for both DFDI and DE methods. For Q' , the merit function for single object observation,

we find that Q'_{DFDI} is consistently higher than Q'_{DE} regardless of the R of the DE instrument under the constraint of total number of pixels, i.e., both the DFDI and DE instrument adopt the same NIR detector. The DE instrument requires using a larger detector in order to reach the same wavelength coverage as the DFDI instrument. Note that the above conclusion is based on the assumption that the number of pixels per spectral order are the same for DFDI and DE. In practice, a DFDI instrument uses ~ 20 pixels to sample spatial direction, i.e., the direction transverse to dispersion direction, while ~ 5 pixels are usually used to sample spatial direction in a DE instrument. However, the ~ 20 pixels sampling is not a requirement for DFDI but rather for the convenience of data reduction. Normally, ~ 7 pixels sample one spatial period of a stellar fringe, which in principle are adequate based on a phase-stepping algorithm provided by Erskine (2003).

If the same detector is used, the spare part of the detector in DFDI can be used for multi-object observations. Consequently, in addition to single-object instrument, we also investigate Q'' , a merit function for multi-object RV measurement for both DFDI and DE. Different conclusions are reached depending on different value of α , an index of the importance of multi-object observation. From a pure photon gain point of view, DFDI and DE instruments have similar Q'' values with Q''_{DFDI} slightly better than Q''_{DE} (a factor of ~ 1.1). From a survey efficiency point of view, a DFDI multi-object instrument is 9 times faster than its counterpart using DE for slow rotating stars ($0 \text{ km} \cdot \text{s}^{-1} \leq V \sin i \leq 2 \text{ km} \cdot \text{s}^{-1}$) and ~ 4 times faster for fast rotators ($V \sin i \geq 10 \text{ km} \cdot \text{s}^{-1}$).

7.2. Application of DFDI

InfraRed Exoplanet Tracker (IRET) is used as an example to demonstrate RV performance with the DFDI method and illustrate how the RV performance is related to other parameters. It is shown that for slow rotators with T_{eff} ranging from 2400K to 3100K, the Q factor is maximized at an OPD of around 18.0 mm. According to predicted photon-limited RV precision, IRET is capable of detecting Earth-like planets in habitable zone around bright M dwarfs if they exist. In our simulations, we consider the photon loss due to optics, CCD detector and the telescope transmission loss of 20%. For the real observation, the total detection efficiency needs to include the atmospheric transmission loss, fiber coupling and seeing losses. It is likely that the overall detection efficiency is a factor of two lower, which requires 2 times longer exposure to reach the same Doppler precision. In addition, the real instrument may have short and long term systematics which affect RV measurement precision. Therefore, the performance of IRET predicted in the paper should be considered as an estimation in an optimistic case.

There may be other practical concerns about the instrument using the DFDI method, most of them are due to the relative low spectral resolution compared to current DE instruments. First of all, an absolute wavelength calibration for a DFDI instrument is not as precise as a DE instrument with a higher spectral resolution. For example, at a spectral resolution of 22,000 for IRET, a line profile with a FWHM of $\sim 0.45 \text{ \AA}$ in Y band is expected. Following the method described in Butler et al. (1996), it corresponds to $136.4 \text{ m} \cdot \text{s}^{-1}$ RV uncertainty at a S/N of 100 if only one

spectral line is used. Ramsey et al. (2010) proposed to use a U-Ne emission lamp as a wavelength calibration source and it has approximately ~ 500 lines in Y band according to their measurement. Therefore, after all the lines in Y band are considered, $\sim 6 \text{ m} \cdot \text{s}^{-1}$ RV uncertainty is introduced in the process of absolute wavelength calibration. In comparison, a DE instrument at R of 110,000 causes $\sim 1.2 \text{ m} \cdot \text{s}^{-1}$ RV uncertainty in an absolute wavelength calibration. However, an absolute wavelength solution is only required for the DE method in order to measure RV drift due to instrument instability, which is measured in a different method in a DFDI instrument. It is similar to a stellar RV measurement, the difference is that the object is switched from a star to an wavelength calibration source. Vertical fringe movement of absorption or emission lines of an RV calibration source is measured instead of centroid movement measurement in a DE instrument. In this case, a DFDI instrument (e.g., IRET, $R=22,000$) is equivalent to a DE instrument with R of 37,000 in terms of Doppler measurement precision (see §4.2). Therefore, instrument RV drift calibration process introduces an RV uncertainty of $\sim 3.5 \text{ m} \cdot \text{s}^{-1}$ for IRET in the example of a U-Ne lamp calibration source. In addition, the RV uncertainty can be further reduced by increasing S/N and number of measurement. Secondly, at a low spectral resolution, it is challenging to perform spectral line profile analysis and thus it requires high-resolution follow-up in order to confirm or exclude a possible detection. Last but not least, in a binary case in which the observed spectrum is blended, two approaches can be used for identification: 1, from measured RV, if the flux ratio is small, similar to the planet companion case, then the lower mass companion can be identified in the measured RV curve even though small flux contamination exists; if the flux ratio is about unity, indicating strong flux contamination, a large RV scattering is expected because this case is not considered and modeled in the current data reduction pipeline; 2, from measured spectrum, even the observed spectrum is a 2-D fringing spectrum in DFDI, we can still de-fringe the spectrum into a 1-D traditional spectrum, on which special treatment can be performed to quantify the blending such as TODCOR (Zucker et al. 2003).

7.3. Telluric Contamination

We develop a quantitative method of estimating telluric line influence on RV uncertainty. We confine the discussion within the context of DFDI method, but it can be readily applied to DE method. We assume different levels of RV fluctuation due to atmospheric behaviors $\delta v_{N,ATM}$ ($5 \text{ m} \cdot \text{s}^{-1}$, $10 \text{ m} \cdot \text{s}^{-1}$ and $20 \text{ m} \cdot \text{s}^{-1}$). After masking a certain portion of the severely contaminated stellar spectrum, optimal RV uncertainty v_{rms} is ~ 3 times worse than the photon-limited RV uncertainty of the stellar spectrum $\delta v_{rms,S}$. At low levels of telluric lines modeling and removing, it requires to mask out about 30% to 50% of a stellar spectrum to reach an optimal RV uncertainty. As telluric line removal becomes more effective, optimal RV uncertainty, δv_{rms} , reaches a smaller value. At a very high level of removal, in which 99% of the strength of telluric lines is removed, i.e., the residual of telluric line modeling is only 1%, telluric line masking becomes unnecessary. The entire wavelength coverage region can be used in RV measurements, and δv_{rms} approaches the fundamental photon-limited RV uncertainty, $\delta v_{rms,S}$.

We acknowledge the support from NSF with grant NSF AST-0705139, NASA with grant NNX07AP14G (Origins), UCF-UF SRI program, DoD ARO Cooperative Agreement W911NF-09-2-0017, Dharma Endowment Foundation and the University of Florida. We thank Mr. Scott Fleming for proofreading this paper draft.

REFERENCES

- Allard, F., Hauschildt, P. H., Alexander, D. R., Tamanai, A., & Schweitzer, A. 2001, *ApJ*, 556, 357
- Bean, J. L., Seifahrt, A., Hartman, H., Nilsson, H., Wiedemann, G., Reiners, A., Dreizler, S., & Henry, T. J. 2010, *ApJ*, 713, 410
- Blake, C. H., Charbonneau, D., & White, R. J. 2010, *ApJ*, 723, 684
- Bouchy, F., Pepe, F., & Queloz, D. 2001, *A&A*, 374, 733
- Bouchy, F., et al. 2009, *ApJ*, 496, 527
- Butler, R. P., Marcy, G. W., Williams, E., McCarthy, C., Dosanji, P., & Vogt, S. S. 1996, *PASP*, 108, 500
- Butler, R. P., Vogt, S. S., Marcy, G. W., Fischer, D. A., Wright, J. T., Henry, G. W., Laughlin, G., & Lissauer, J. J. 2004, *ApJ*, 617, 580
- Charbonneau, D., et al. 2009, *Nature*, 462, 891
- Endl, M., Cochran, W. D., Kürster, M., Paulson, D. B., Wittenmyer, R. A., MacQueen, P. J., & Tull, R. G. 2006, *ApJ*, 649, 436
- Erskine, D. J. 2003, *PASP*, 115, 255
- Erskine, D. J., & Ge, J. 2000, in *Astronomical Society of the Pacific Conference Series*, Vol. 195, *Imaging the Universe in Three Dimensions*, ed. W. van Breugel & J. Bland-Hawthorn, 501–+
- Figueira, P., Pepe, F., Lovis, C., & Mayor, M. 2010, *A&A*, 515, A106+
- Fleming, S. W., et al. 2010, *ApJ*, 718, 1186
- Forveille, T., et al. 2009, *A&A*, 493, 645
- Ge, J., E. D. J. . R. M. 2002a, *PASP*, 114, 1016
- Ge, J. 2002b, *ApJ*, 571, 165
- Ge, J., et al. 2006, *ApJ*, 648, 683

- Haghighipour, N., Vogt, S. S., Butler, R. P., Rivera, E. J., Laughlin, G., Meschiari, S., & Henry, G. W. 2010, *ApJ*, 715, 271
- Hauschildt, P. H., Allard, F., & Baron, E. 1999, *ApJ*, 512, 377
- Howard, A. W., et al. 2010, *ArXiv e-prints*
- Jenkins, J. S., Ramsey, L. W., Jones, H. R. A., Pavlenko, Y., Gallardo, J., Barnes, J. R., & Pinfield, D. J. 2009, *ApJ*, 704, 975
- Jiang, P., Ge, J., Liu, Q., & Wang, J. 2011, *In Prep.*
- Johnson, J. A., et al. 2010, *PASP*, 122, 149
- Lee, B. L., et al. 2011, *ApJ*, 728, 32
- Lépine, S., & Shara, M. M. 2005, *AJ*, 129, 1483
- Lord, S. D. 1992, *NASA Technical Memorandum*
- Maillard, J. P. 1996, *Appl. Opt.*, 35, 2734
- Mosser, B., Maillard, J.-P., & Bouchy, F. 2003, *PASP*, 115, 990
- Muirhead, P. S., et al. 2011, *ArXiv e-prints*
- Ramsey, L. W., Mahadevan, S., Redman, S., Bender, C., Roy, A., Zonak, S., Sigurdsson, S., & Wol-szczan, A. 2010, in *Society of Photo-Optical Instrumentation Engineers (SPIE) Conference Series*, Vol. 7735, *Society of Photo-Optical Instrumentation Engineers (SPIE) Conference Series*
- Reiners, A., Bean, J. L., Huber, K. F., Dreizler, S., Seifahrt, A., & Czesla, S. 2010, *ApJ*, 710, 432
- Vacca, W. D., Cushing, M. C., & Rayner, J. T. 2003, *PASP*, 115, 389
- van Eyken, J. C., Ge, J., & Mahadevan, S. 2010, *ApJS*, 189, 156
- Wright, J. T., Marcy, G. W., Butler, R. P., & Vogt, S. S. 2004, *ApJS*, 152, 261
- Zechmeister, M., Kürster, M., & Endl, M. 2009, *A&A*, 505, 859
- Zhao, B., Ge, J., Nguyen, D. C., Wang, J., & Groot, J. 2010, in *Society of Photo-Optical Instrumentation Engineers (SPIE) Conference Series*, Vol. 7735, *Society of Photo-Optical Instrumentation Engineers (SPIE) Conference Series*
- Zucker, S., Mazeh, T., Santos, N. C., Udry, S., & Mayor, M. 2003, *A&A*, 404, 775

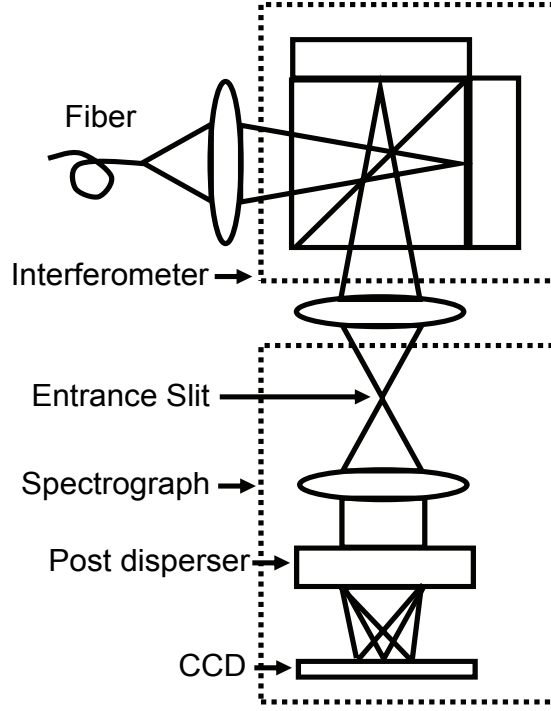


Fig. 1.— A schematic layout of an RV instrument using the DFDI method.

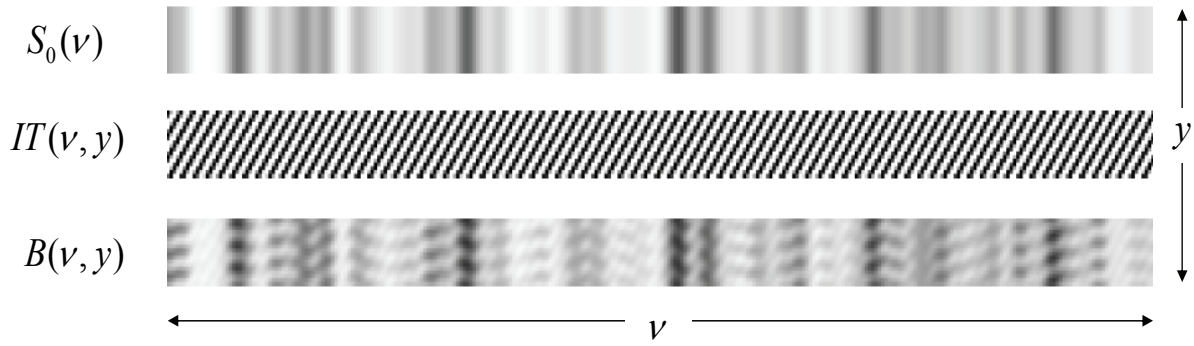


Fig. 2.— DFDI Illustration. $S_0(\nu)$ is a stellar spectrum; $IT(\nu, y)$ is interferometer transmission; $B(\nu, y)$ is the image taken at a 2-D detector. ν is optical frequency and y is coordinate of slit direction. DFDI measures RV by monitoring phase shift of stellar absorption line fringes in the y direction (the slit direction).

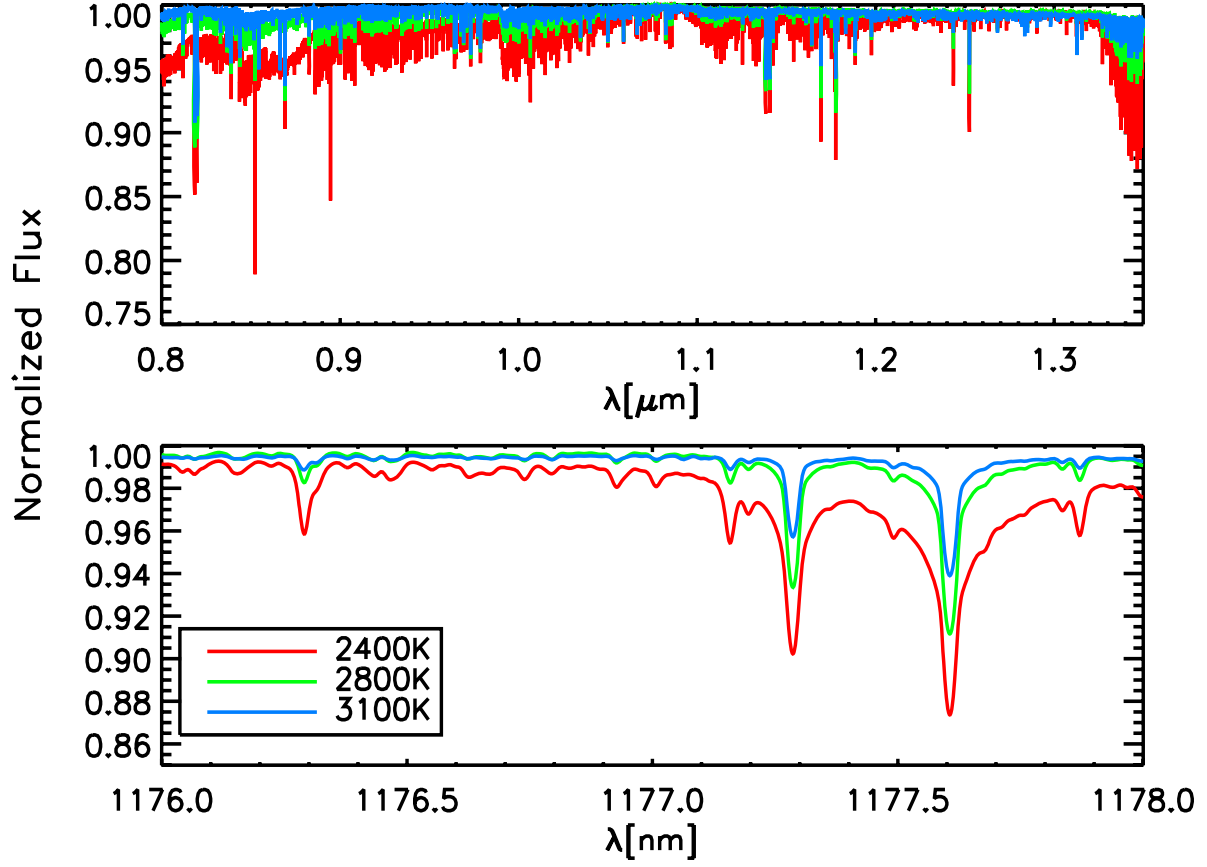


Fig. 3.— Examples of synthetic M dwarf stellar spectra ($V \sin i = 0 \text{ km} \cdot \text{s}^{-1}$), which are generated by PHOENIX (Hauschildt et al. 1999; Allard et al. 2001). The top panel shows the spectra between 0.8-1.35 μm , the bottom panel shows an enlarged spectral region around 1177 nm showing stellar line profiles.

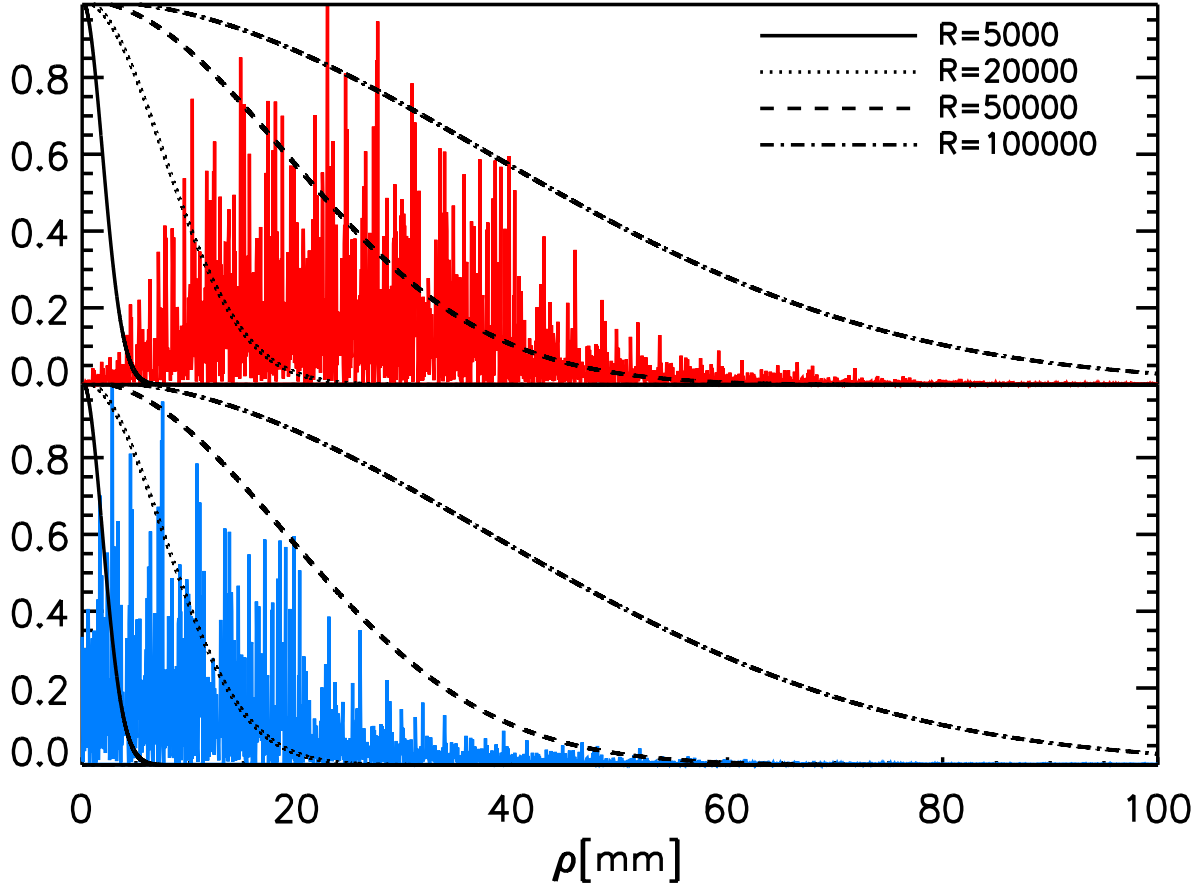


Fig. 4.— Top: power spectrum of derivatives of stellar spectrum, $\mathcal{F}[dS_0/d\nu]$, with $SRF(\rho) = \mathcal{F}[LSF(\nu, R)]$ for different R overplotted, where LSF is line spread function; Bottom: $\mathcal{F}[dS_0/d\nu]$ shifted by $\Delta\rho = 20\text{mm}$ using a fixed-delay Michelson interferometer. The SRF s for different R are overplotted.

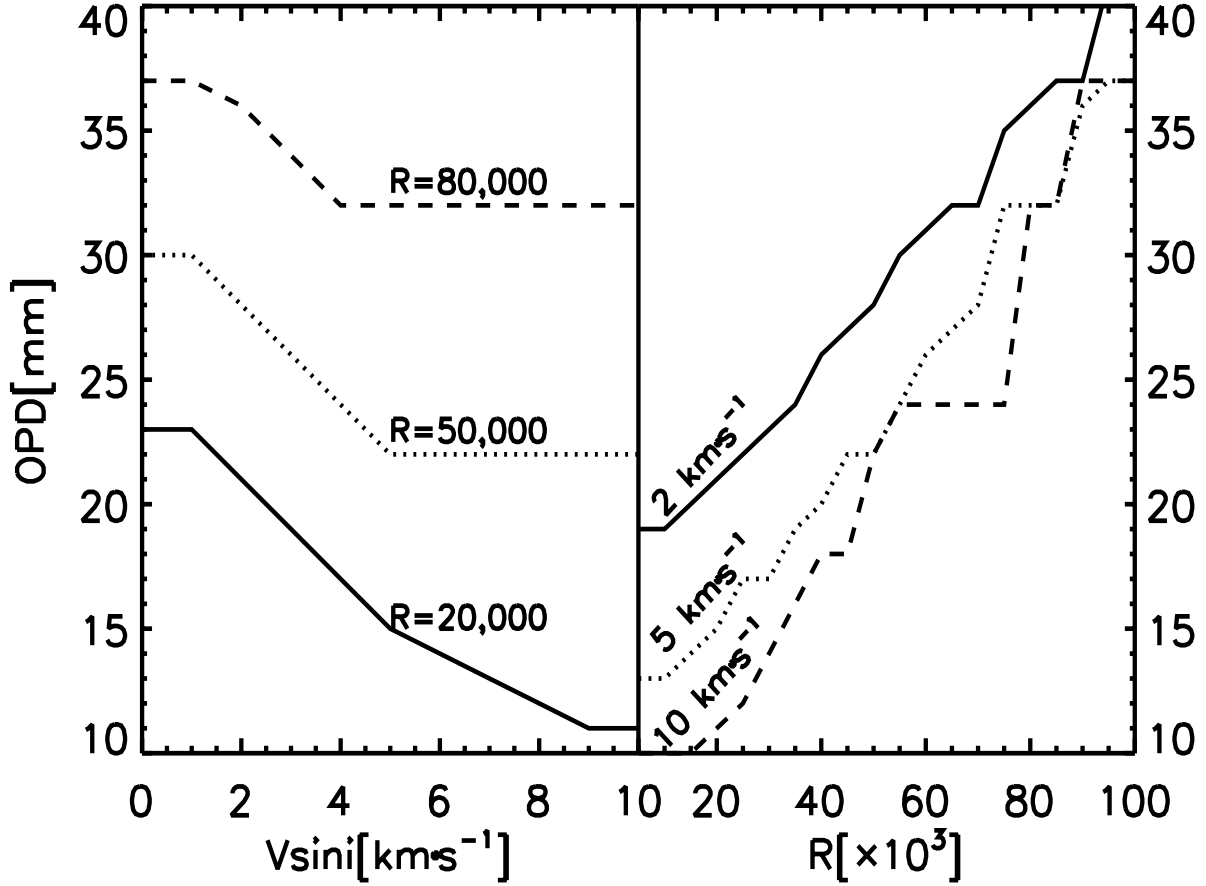


Fig. 5.— Optimal OPD correlation with $V \sin i$ (left) and spectral resolution R (right). Optimal OPD for $R=20,000$ (solid), $50,000$ (dotted), $80,000$ (dashed) are used on the left panel. $V \sin i=2$ (solid), 5 (dotted), 10 (dashed) $\text{km} \cdot \text{s}^{-1}$ are assumed on the right panel. Complete results of optimal OPD can be found in Table 1. T_{eff} influence on optimal OPD is not significant, $T_{\text{eff}}=2800$ K is adopted in the plot.

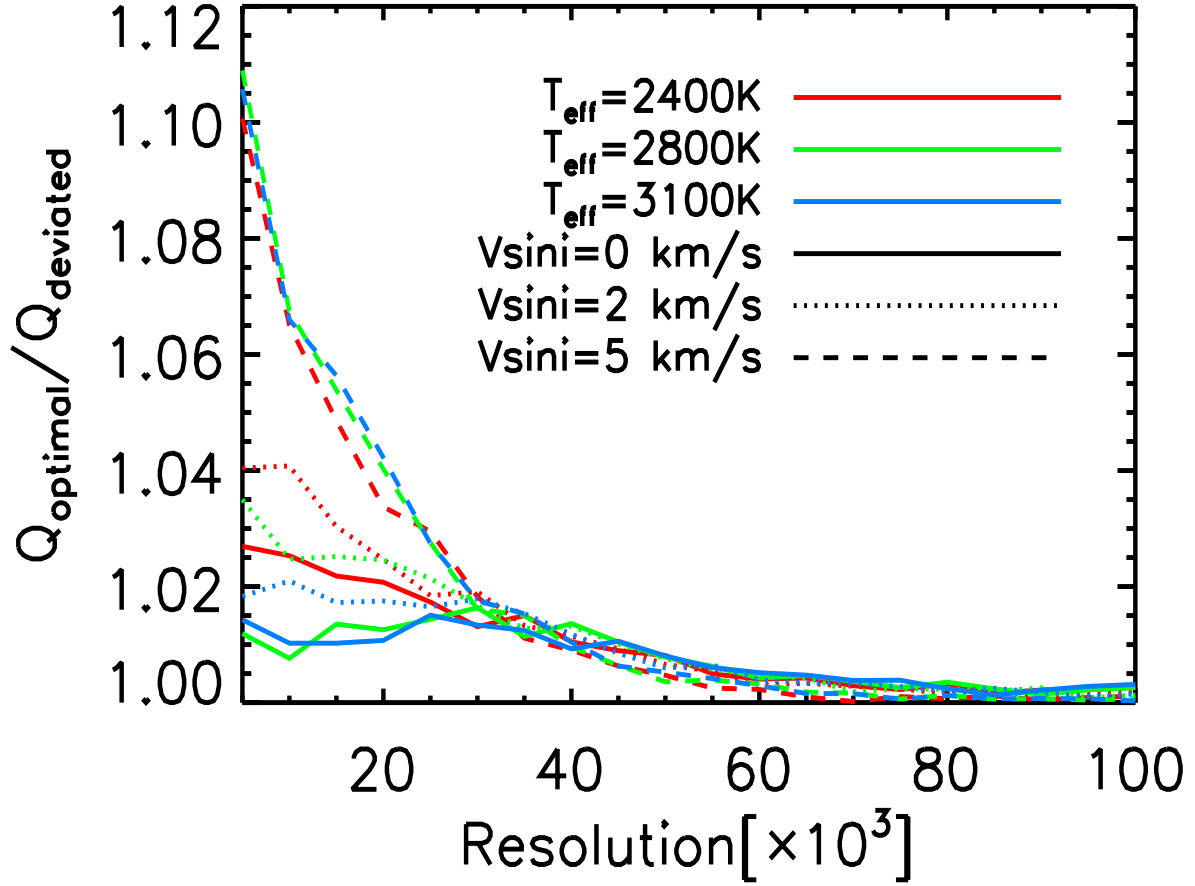


Fig. 6.— Ratio of Q_{optimal} and Q_{deviated} as a function of spectral resolution, where Q_{optimal} is Q factor at optimal OPD and Q_{deviated} is Q factor when OPD is deviated from Q_{optimal} by 5 mm. Different line styles represent different $V \sin i$ while colors indicate different T_{eff} .

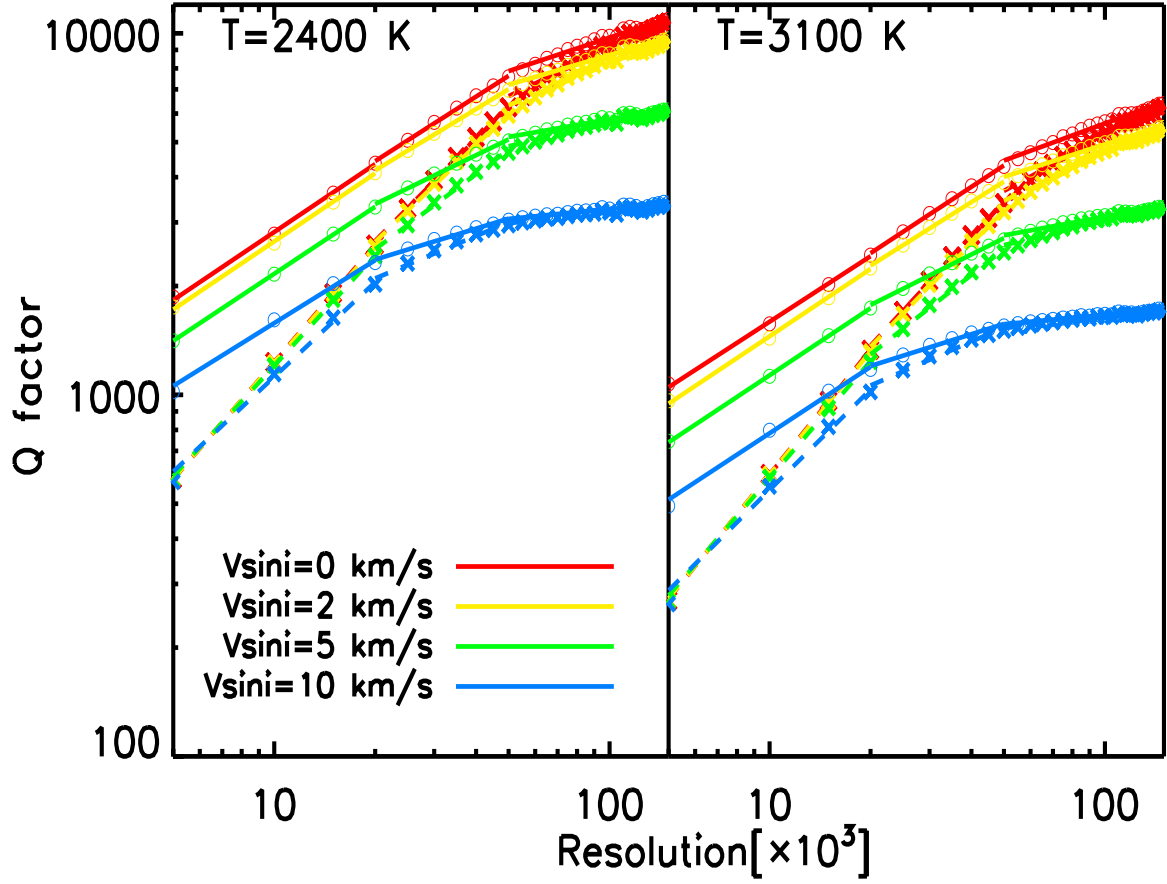


Fig. 7.— Q factor as a function of spectral resolution. (left: $T_{\text{eff}} = 2400 \text{ K}$; right: $T_{\text{eff}} = 3100 \text{ K}$. Open circles represent Q_{DFDI} ; crosses represent Q_{DE} ; solid lines are best power-law fits for Q_{DFDI} ; dashed lines are best power-law fits for Q_{DE})

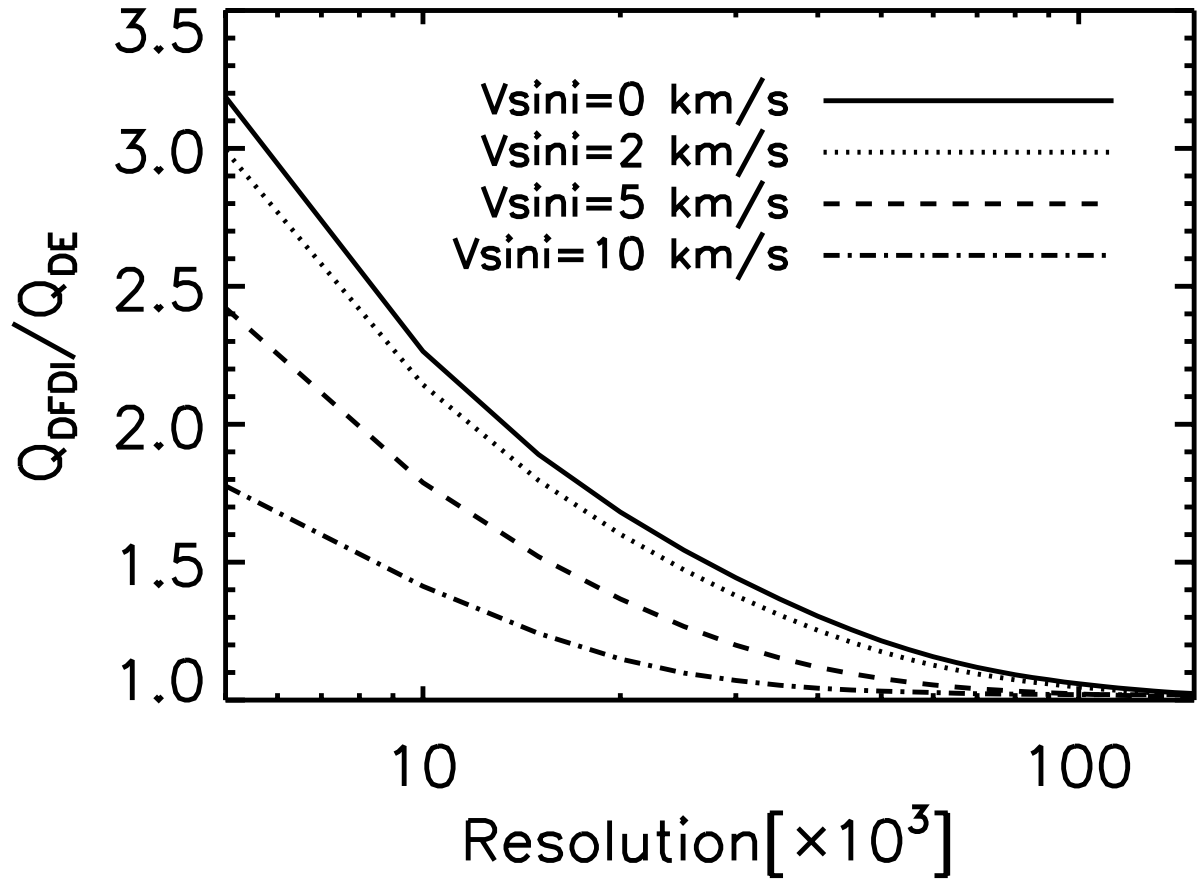


Fig. 8.— Improvement of Q_{DFDI} over Q_{DE} as a function of spectral resolution.

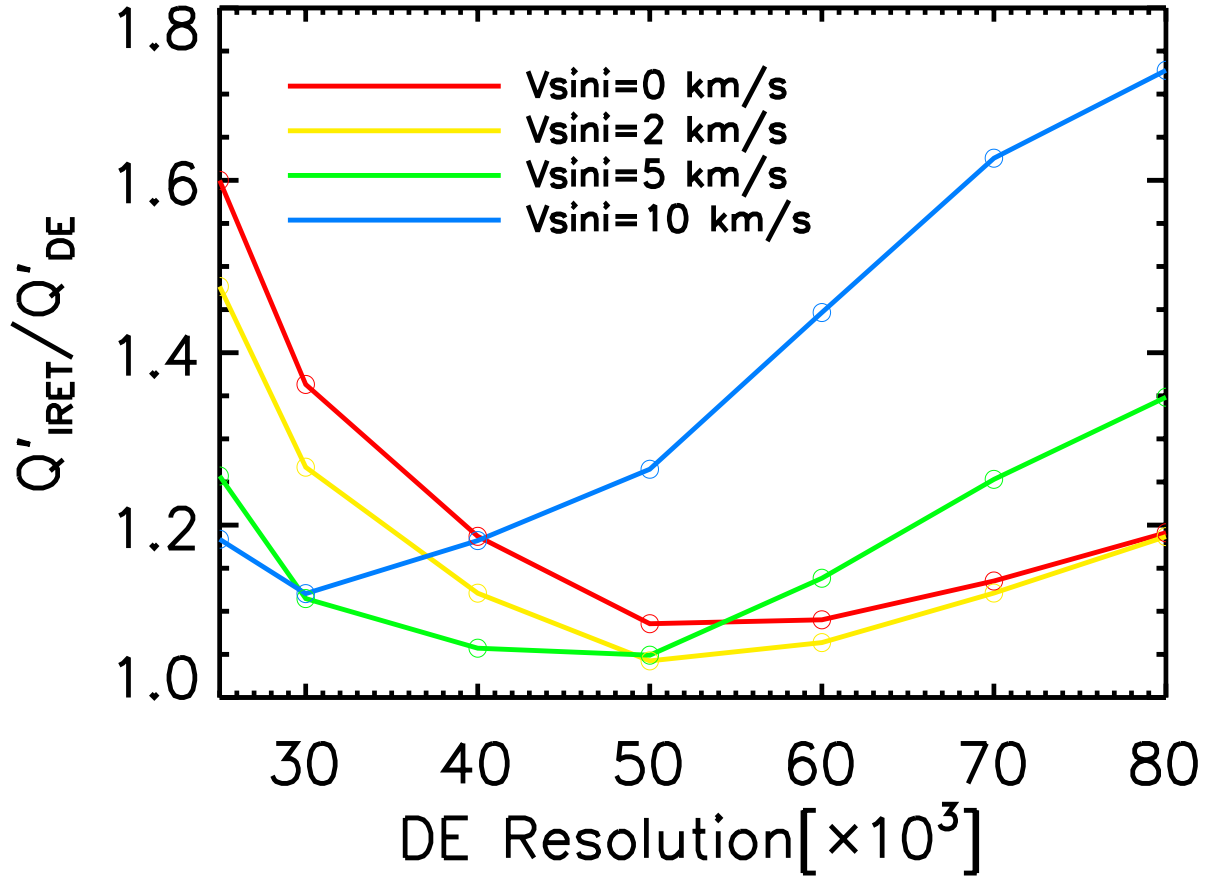


Fig. 9.— Comparison of Q'_{IRET} and Q'_{DE} at different R . Note that $Q' = Q \cdot \sqrt{N_e^-}$. Different color represents different rotational velocity.

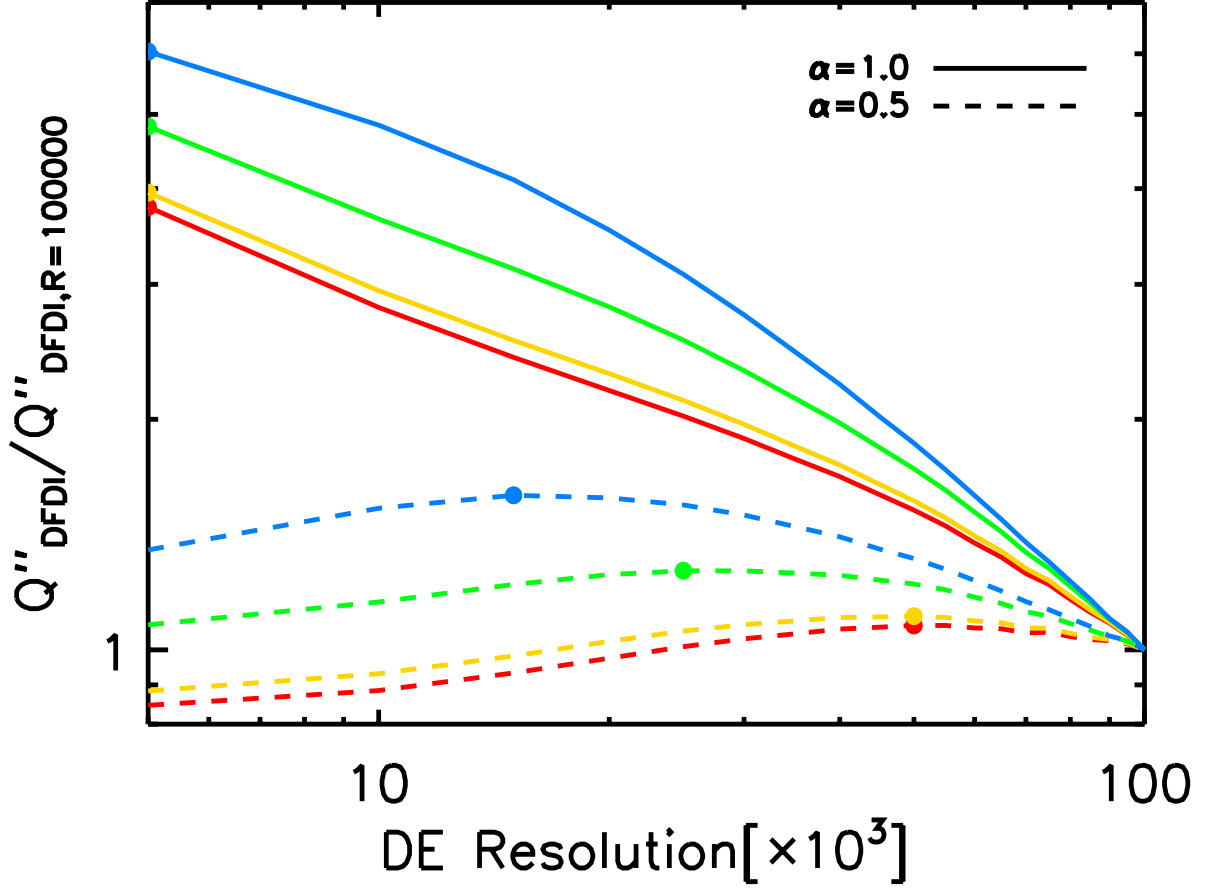


Fig. 10.— Comparison of Q''_{DFDI} and $Q''_{\text{DFDI}, R=100,000}$ at different R . Note that $Q'' = Q \cdot \sqrt{N_{e-}} \cdot N_{obj}^\alpha$. The maximum of each curve is indicated by filled circle. Different color represents different rotational velocity, the same as Fig. 9.

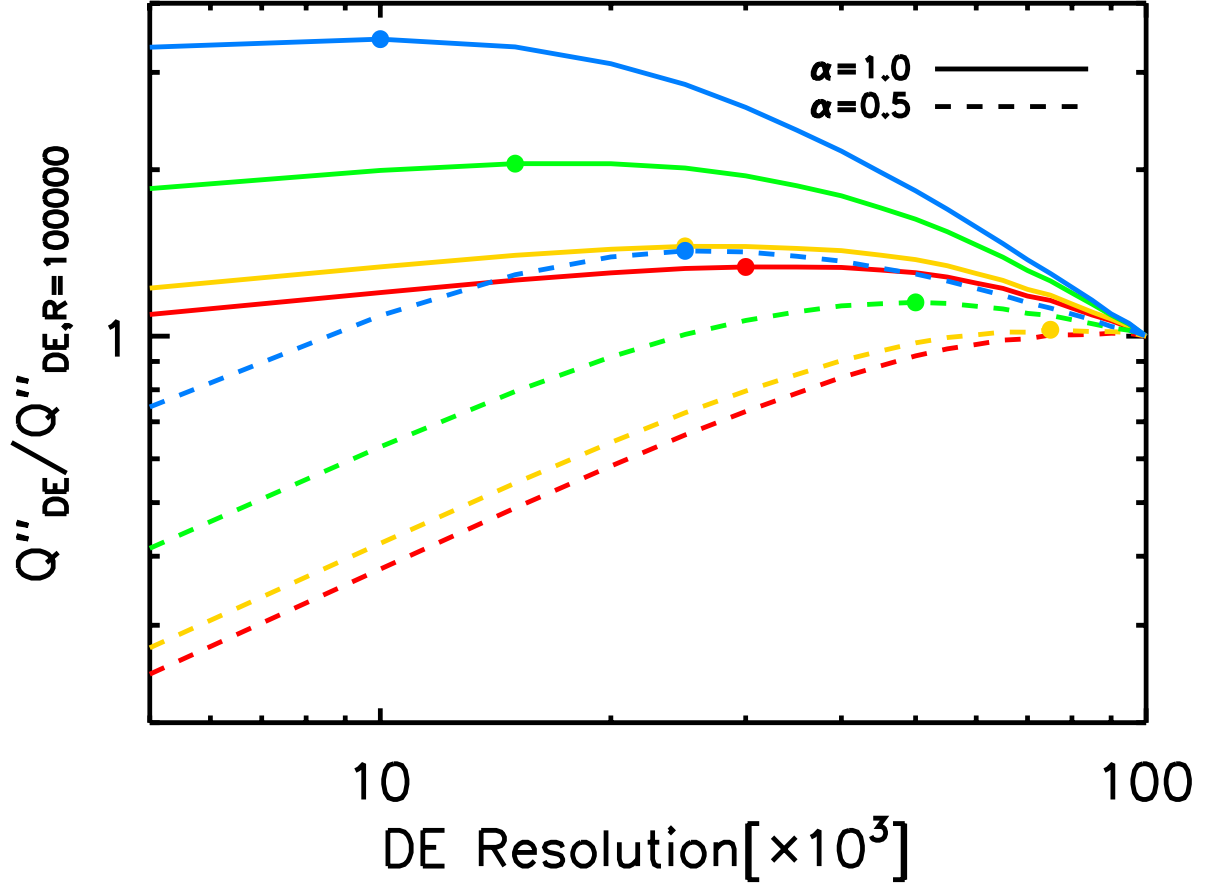


Fig. 11.— Comparison of Q''_{DE} and $Q''_{\text{DE}, R=100,000}$ at different R . Note that $Q'' = Q \cdot \sqrt{N_{e-}} \cdot N_{obj}^{\alpha}$. The maximum of each curve is indicated by filled circle. Different color represents different rotational velocity, the same as Fig. 9.

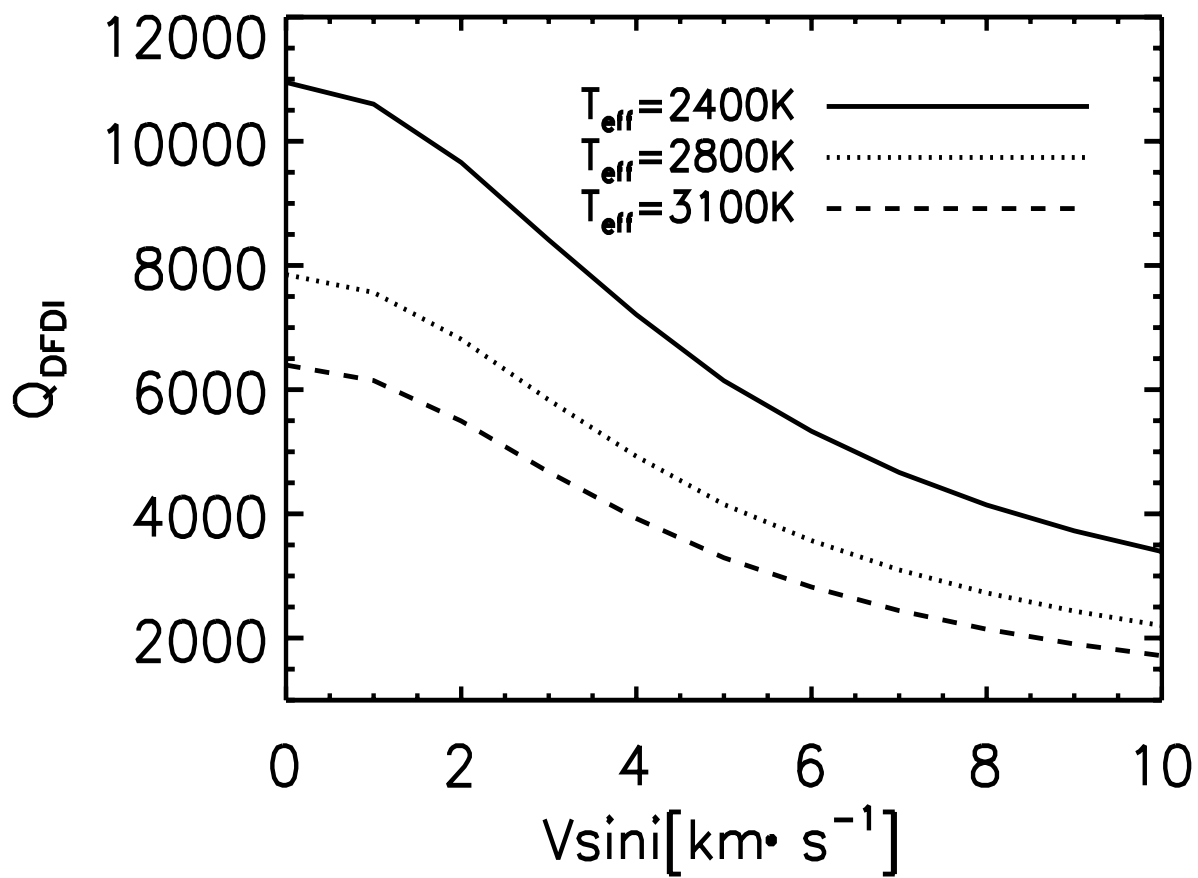


Fig. 12.— Q_{DFDI} as a function of $V \sin i$.

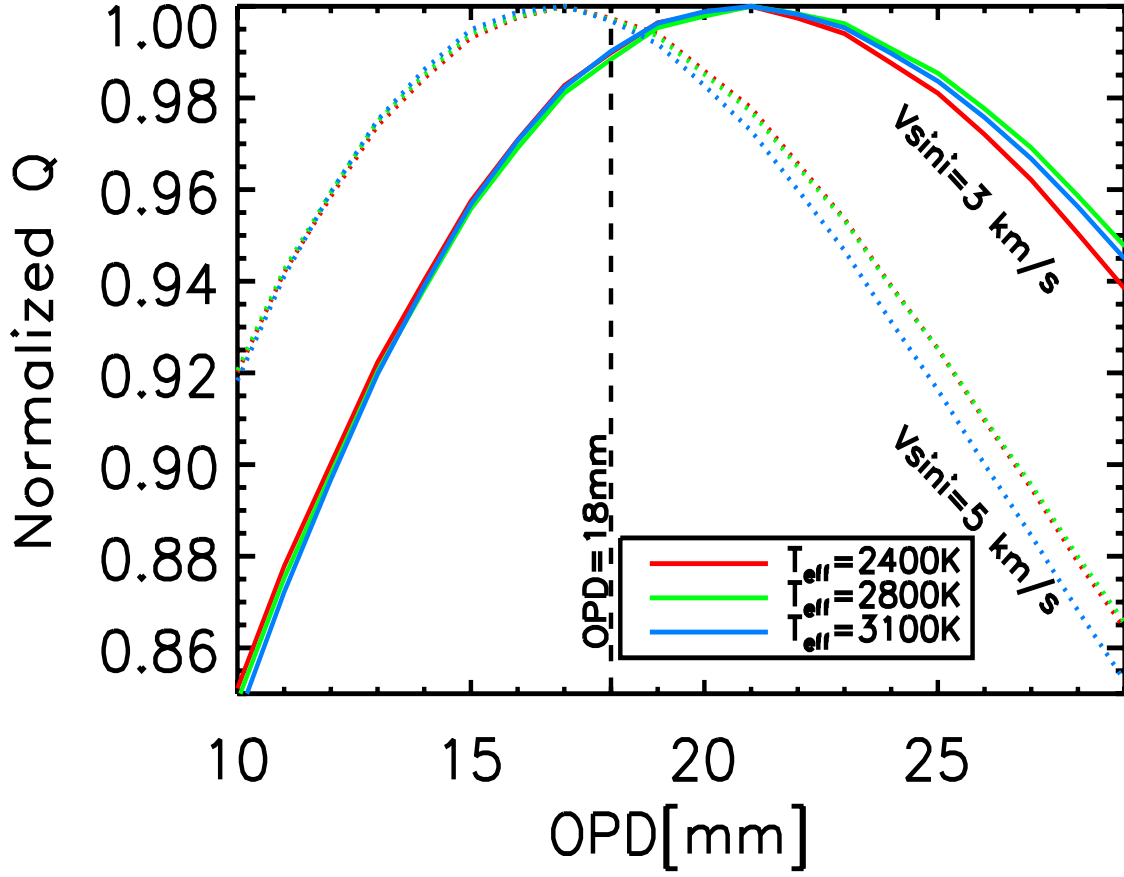


Fig. 13.— OPD optimization for IRET. OPD is optimized at $R = 22,000$, $V \sin i$ between $3 \text{ km} \cdot \text{s}^{-1}$ and $5 \text{ km} \cdot \text{s}^{-1}$.

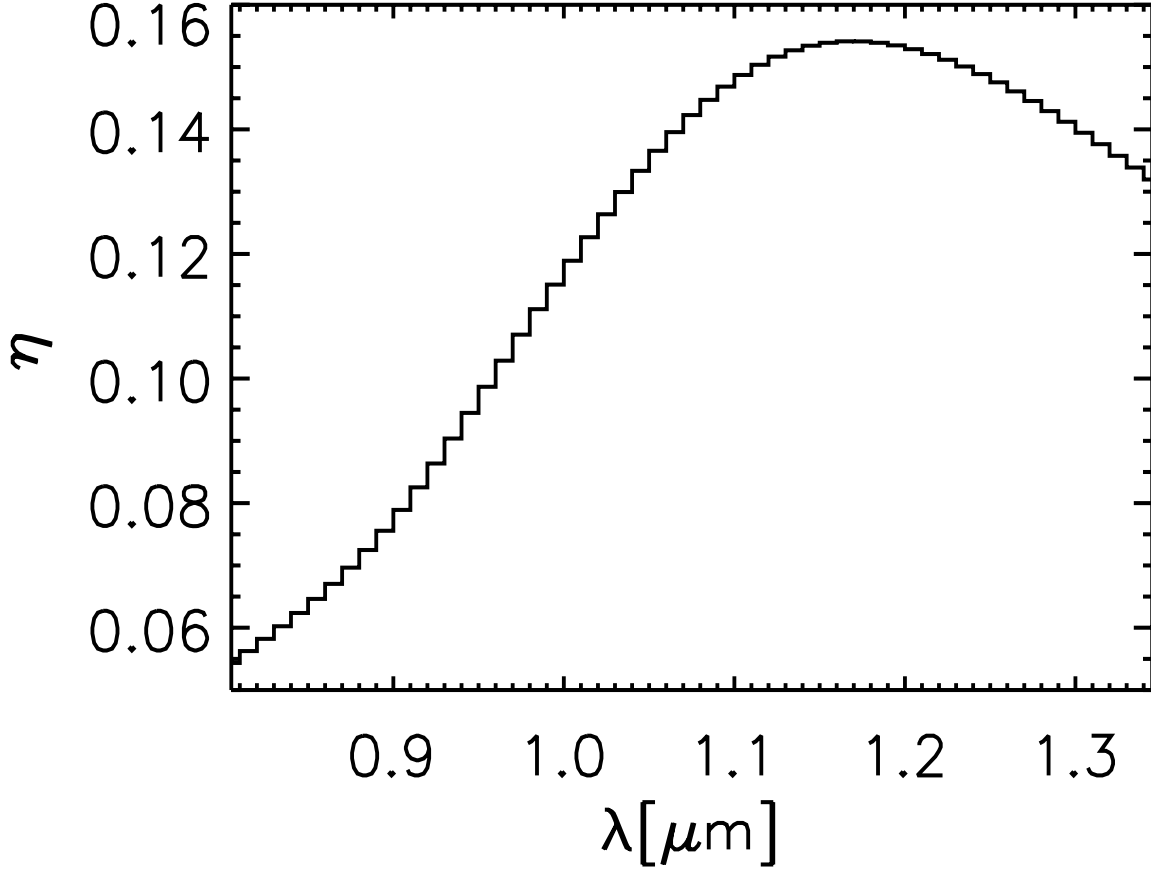


Fig. 14.— Instrument throughput η as a function of wavelength (800 to 1350 nm). The telescope transmission is 80%. It does not include atmospheric transmission, fiber coupling, transmission and seeing losses.

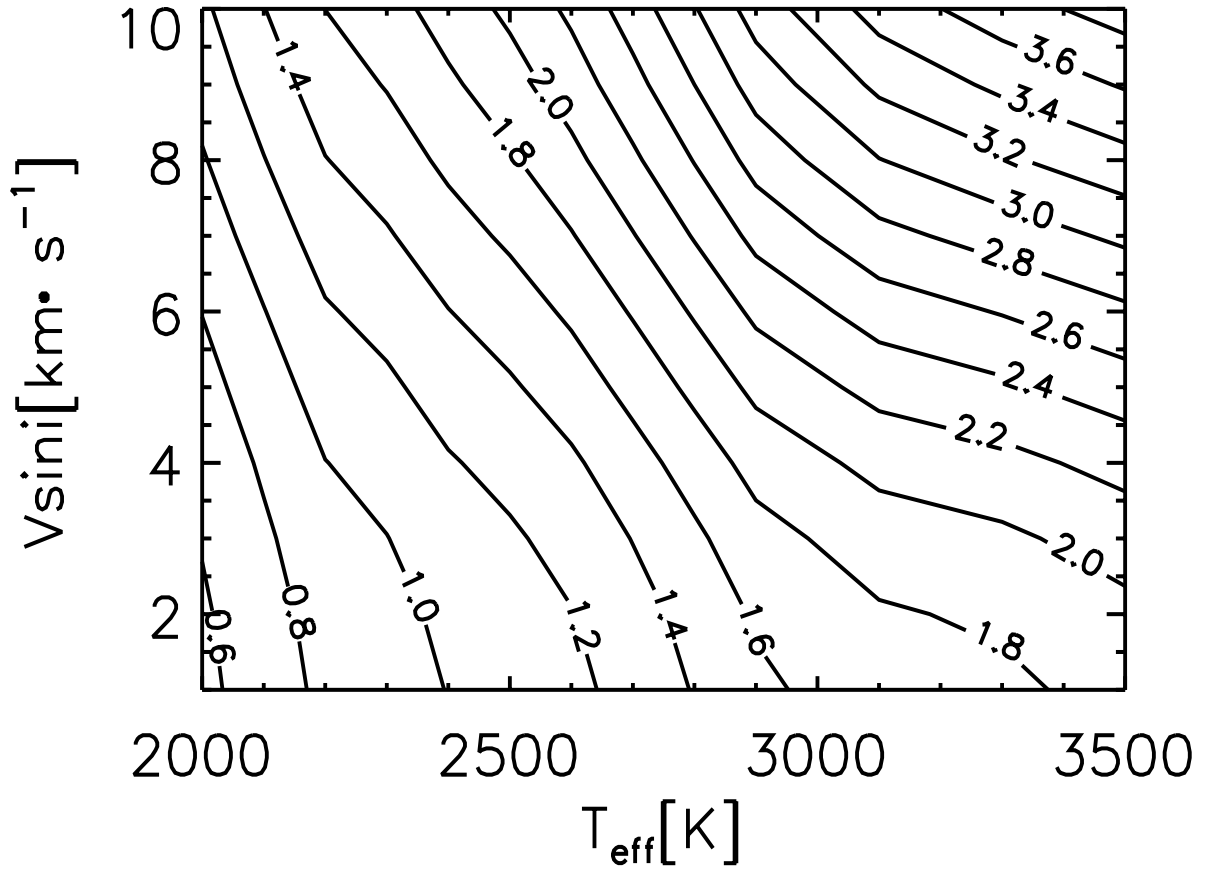


Fig. 15.— Predicted photon-limited RV uncertainty contours (in $\text{m} \cdot \text{s}^{-1}$) for IRET. The assumption in calculation includes: 1) $t_{\text{exp}} = 30$ min; 2) $m_J = 9$; 3) η as shown in Fig. 14.

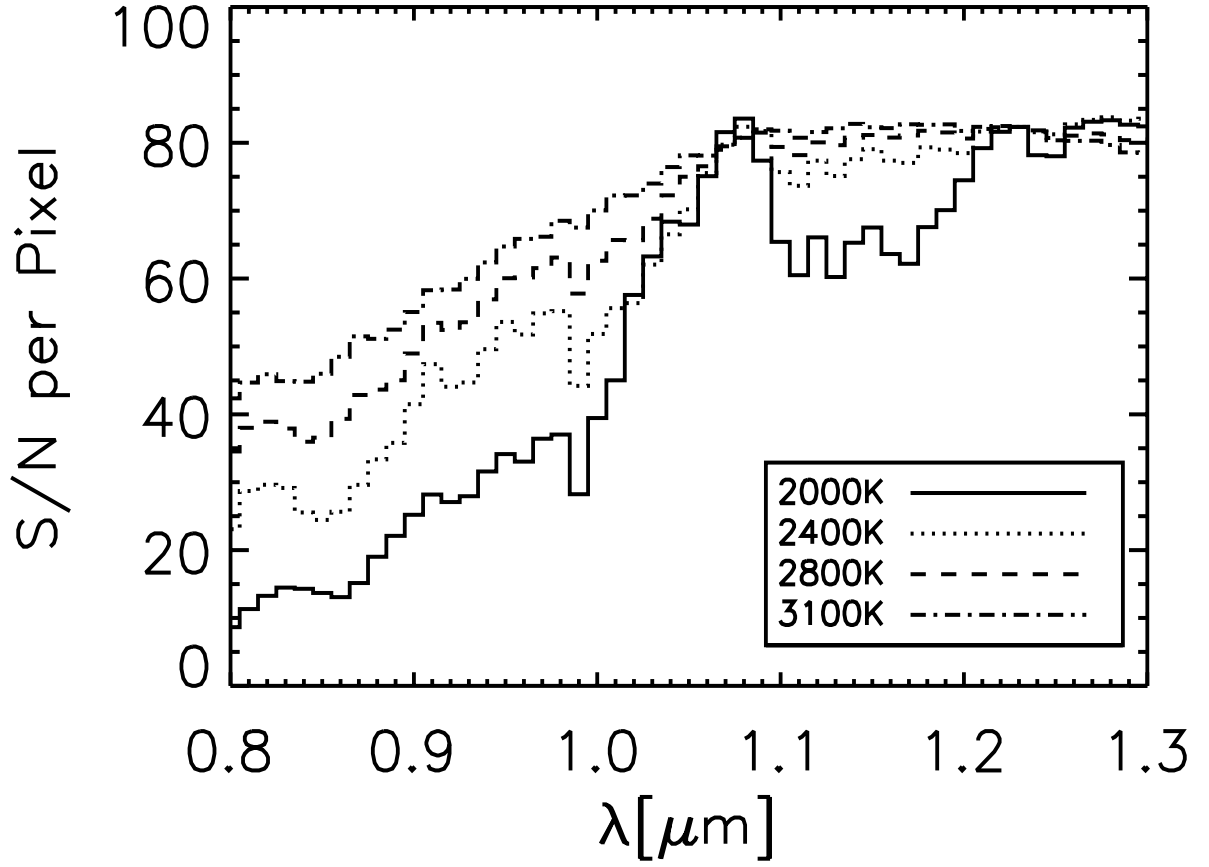


Fig. 16.— S/N per pixel as a function of wavelength. The assumption in calculation includes: 1) $t_{\text{exp}} = 30$ min; 2) $m_J = 9$; 3) η as shown in fig 14. IRET is designed to have 4.2 pixels to sample one RE and 25 pixels to sample fringes in the slit direction in each spectral channel.

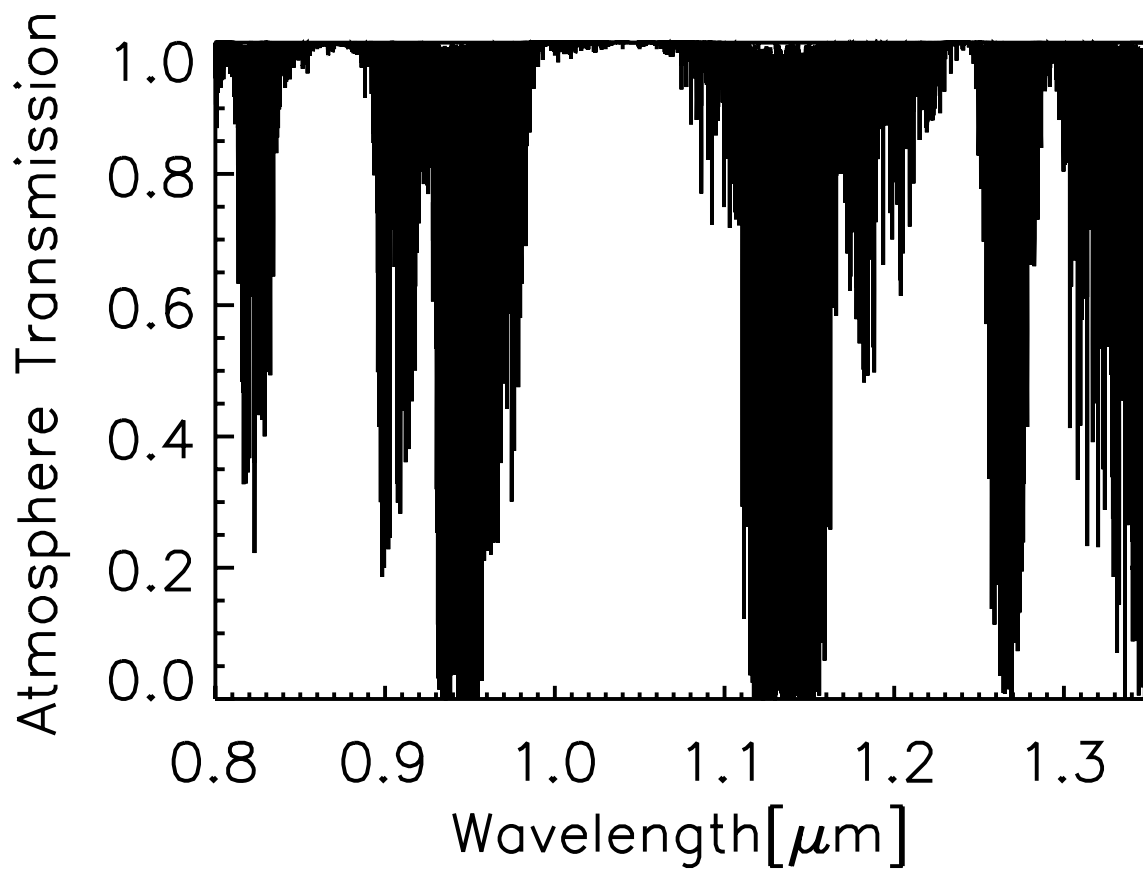


Fig. 17.— Atmosphere transmission (AT) as a function of wavelength (Generated by ATRAN (Lord 1992)).

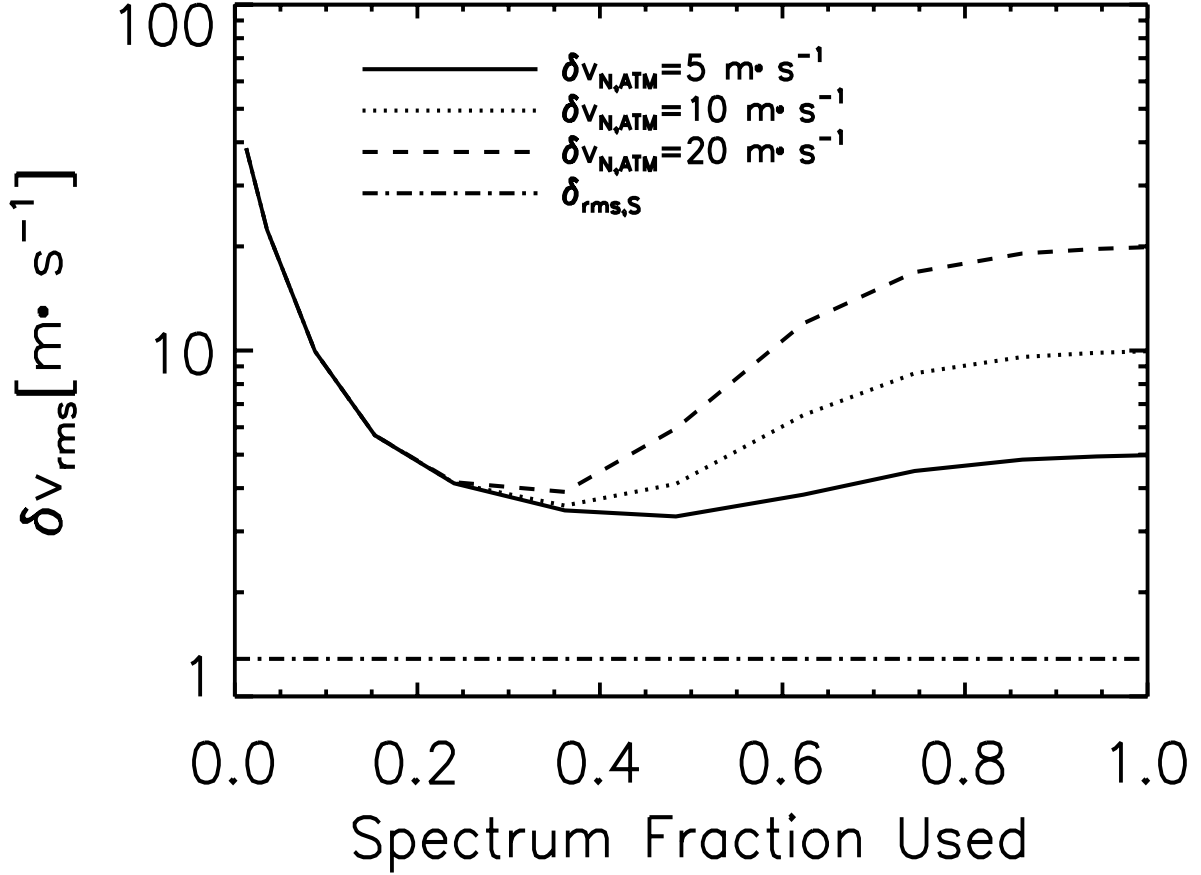


Fig. 18.— Predicted RV uncertainty δv_{rms} as a function of the fraction of stellar spectrum used in RV measurements when applying the telluric line masking technique. We assume $T_{\text{eff}}=2400 \text{ K}$ and $V \sin i$ of $5 \text{ km} \cdot \text{s}^{-1}$. Different levels of atmosphere RV fluctuation are indicated by different line styles. $\delta v_{rms,S}$ (dash-dotted line), the fundamental photon-limited RV uncertainty determined by an intrinsic stellar spectrum for a complete wavelength coverage from 800 to 1350 nm, is plotted for comparison.

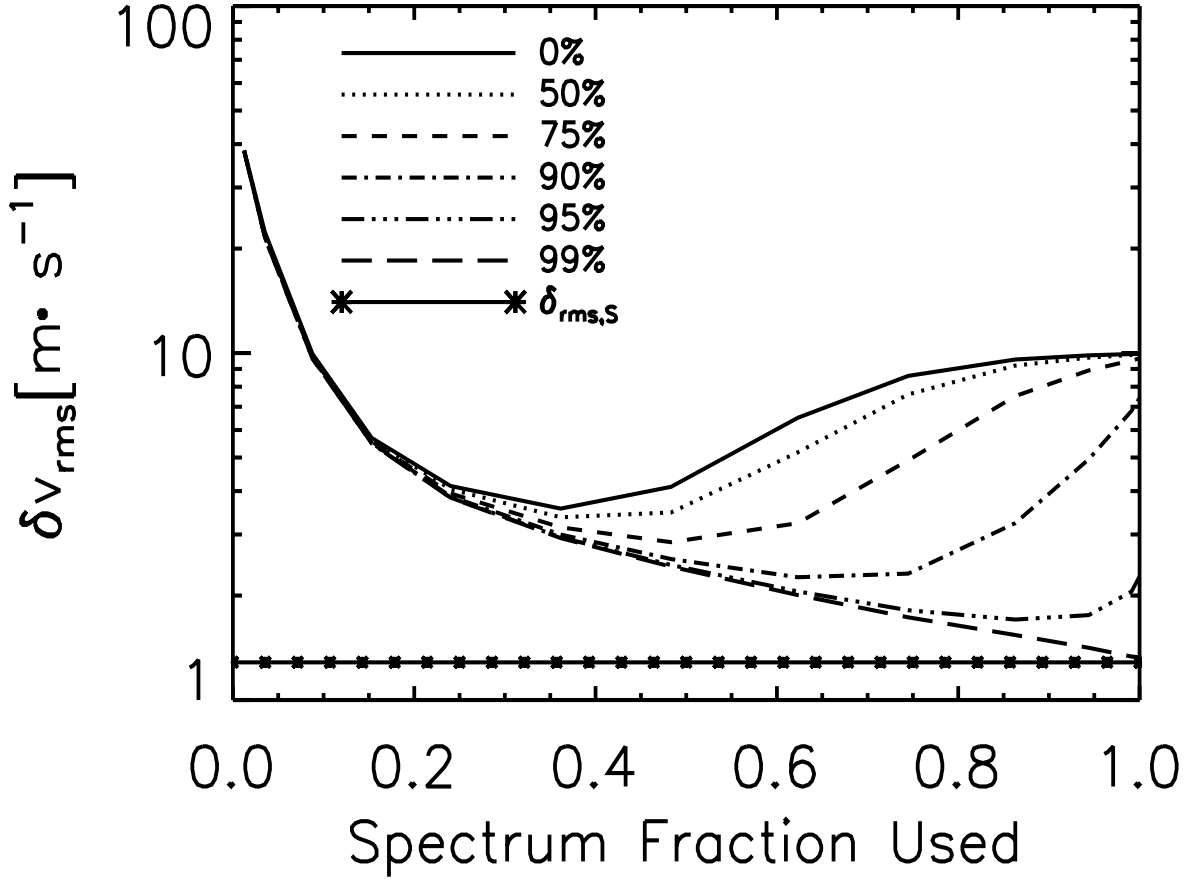


Fig. 19.— Predicted RV uncertainty as a function of fraction of stellar spectrum used in RV measurements when applying the telluric line modeling and removing technique. We assume $T_{\text{eff}}=2400$ K and $V \sin i$ of $5 \text{ km} \cdot \text{s}^{-1}$. Asterisks connected by solid line represent the fundamental photon-limited RV uncertainty. Different line styles represent different level of telluric lines removal (i.e, removed telluric line strength). $\delta v_{N,ATM}=10 \text{ m} \cdot \text{s}^{-1}$ is assumed in the calculations.

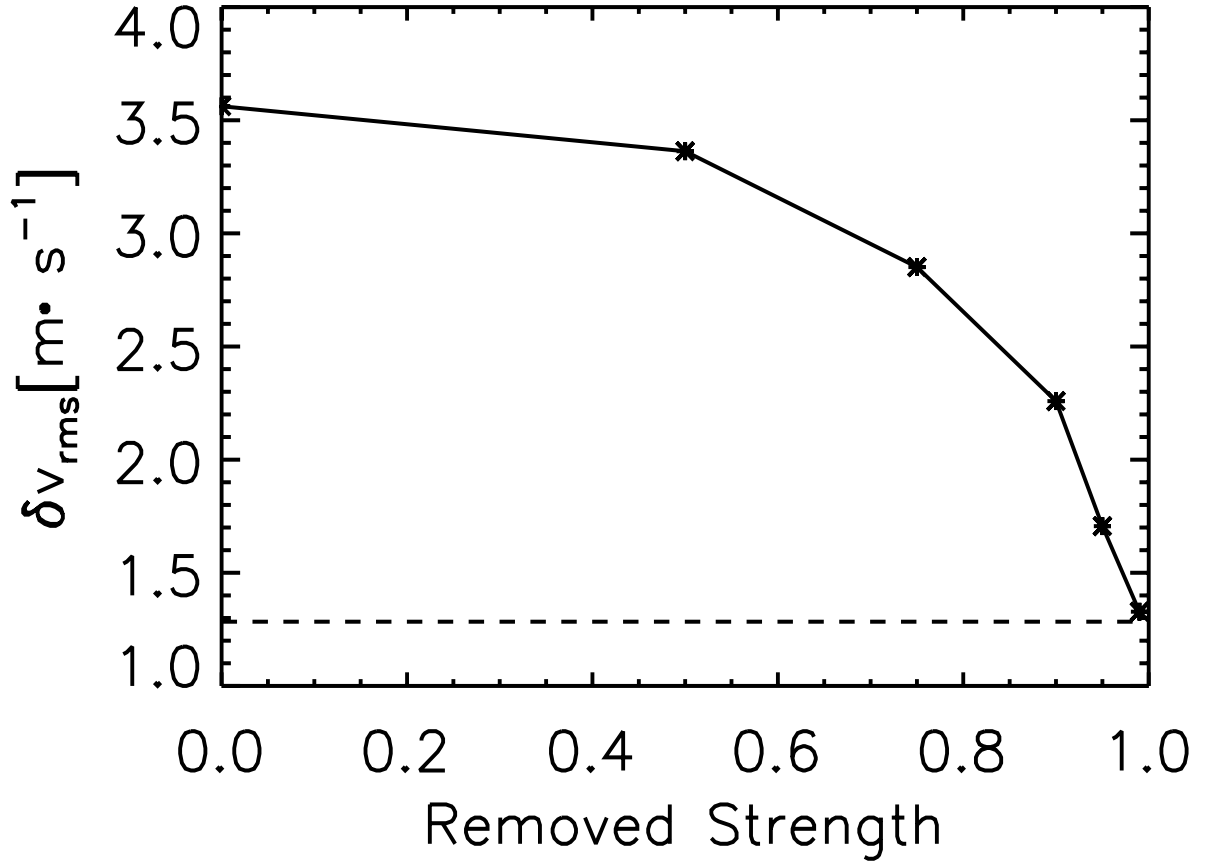


Fig. 20.— Predicted optimal RV uncertainty as a function of removed telluric line strength. Dashed line represents the fundamental photon-limited RV uncertainty, $v_{\text{rms},S}$.

Table 1. OPD choice as a function of R and $V \sin i$ at different T_{eff}

R	$V \sin i$ [km · s ⁻¹]										
	0	1	2	3	4	5	6	7	8	9	10
5,000	19,27,29	19,19,28	19,19,19	15,15,17	15,15,15	13,13,13	11,12,12	10,11,11	10,10,10	10,10,10	10,10,10
10,000	21,23,27	19,21,26	19,19,20	17,17,17	15,15,15	13,13,13	11,12,12	11,11,11	10,10,10	10,10,10	10,10,10
15,000	21,23,26	21,22,23	19,20,20	17,17,17	15,15,15	14,14,14	13,13,13	12,11,11	11,11,11	11,10,10	10,10,10
20,000	22,23,26	21,23,24	20,21,21	19,19,19	17,17,17	15,15,15	14,14,14	13,13,13	12,12,12	11,11,11	11,11,11
25,000	23,24,26	23,24,25	21,22,22	19,20,20	19,18,18	17,17,16	16,15,15	14,14,14	14,13,13	14,13,12	12,12,12
30,000	24,26,26	24,25,26	23,23,24	21,21,21	19,19,19	18,17,17	17,16,16	16,15,15	14,14,14	14,14,14	14,14,14
35,000	26,26,28	26,26,26	24,24,25	22,22,23	21,21,20	19,19,19	19,18,17	17,17,17	16,16,16	16,16,16	16,16,15
40,000	27,28,28	27,27,28	26,26,26	24,24,24	22,22,22	21,20,20	19,19,19	19,18,18	19,18,18	19,18,18	19,18,16
45,000	29,29,30	28,28,29	27,27,28	25,25,26	24,23,23	22,22,21	22,20,20	22,20,20	22,20,18	22,18,18	22,18,18
50,000	30,30,31	29,30,30	28,28,28	27,26,26	24,24,24	24,22,23	22,22,22	22,22,22	22,22,22	22,22,22	24,22,22
55,000	32,32,32	31,31,32	30,30,30	27,28,28	27,26,26	24,24,24	24,24,24	24,24,22	24,24,22	24,24,22	24,24,24
60,000	32,32,34	32,32,33	32,31,32	29,28,28	27,27,26	27,26,26	24,24,24	24,24,24	24,24,24	24,24,24	24,24,24
65,000	34,34,35	34,34,34	32,32,32	32,30,30	29,28,28	27,27,26	27,26,26	27,24,26	24,24,26	24,24,24	24,24,24
70,000	35,35,36	35,35,36	34,32,34	32,32,32	32,30,30	32,28,28	27,28,28	27,28,26	27,24,26	24,24,26	24,24,26
75,000	37,36,37	37,36,37	35,35,35	32,32,32	32,32,32	32,32,32	32,32,28	32,32,28	32,32,32	32,32,32	32,24,32
80,000	37,37,39	37,37,37	37,36,36	35,34,35	35,32,32	32,32,32	32,32,32	32,32,32	35,32,32	35,32,32	35,32,32
85,000	40,39,41	40,39,39	37,37,37	37,36,36	35,32,32	35,32,32	35,32,32	35,32,32	35,32,32	35,32,32	35,32,32
90,000	40,41,41	40,41,41	40,37,39	37,36,36	37,36,36	37,36,36	35,32,36	35,32,36	37,37,36	37,37,36	37,37,36
95,000	41,41,41	41,41,41	40,41,41	40,37,37	37,37,36	37,37,36	37,37,36	37,37,36	37,37,37	37,37,37	37,37,37
100,000	41,41,41	41,41,41	40,41,41	40,40,41	37,37,37	37,37,36	37,37,36	37,37,37	37,37,37	37,37,37	37,37,37
105,000	41,41,41	41,41,41	41,41,41	40,41,41	40,40,41	37,37,37	37,37,37	37,37,37	37,37,37	37,37,37	37,37,37
110,000	41,41,41	41,41,41	40,41,41	40,41,41	40,41,41	37,41,41	37,37,41	37,37,37	37,37,37	37,37,37	37,37,37
115,000	41,41,41	41,41,41	41,41,41	40,41,41	40,41,41	37,41,41	37,41,41	37,37,41	37,37,37	37,37,37	37,37,37
120,000	41,41,41	41,41,41	41,41,41	40,41,41	40,41,41	37,41,41	37,41,41	37,37,41	37,37,37	37,37,37	37,37,37
125,000	41,41,41	41,41,41	41,41,41	40,41,41	40,41,41	37,41,41	37,41,41	37,37,41	37,37,37	37,37,37	37,37,37
130,000	41,41,41	41,41,41	40,41,41	40,41,41	40,41,41	37,41,41	37,41,41	37,37,41	37,37,37	37,37,37	37,37,37
135,000	41,41,41	41,41,41	40,41,41	40,41,41	40,41,41	37,41,41	37,41,41	37,37,41	37,37,37	37,37,37	37,37,37
140,000	41,41,41	41,41,41	40,41,41	40,41,41	40,41,41	37,41,41	37,41,41	37,41,41	37,37,41	37,37,37	37,37,37
145,000	41,41,41	41,41,41	40,41,41	40,41,41	40,41,41	40,41,41	37,41,41	37,41,41	37,41,41	37,41,41	37,41,41
150,000	41,41,41	41,41,41	40,41,41	40,41,41	40,41,41	40,41,41	37,41,41	37,41,41	37,41,41	37,41,41	37,41,41

Note. — The first number in each tab is the optimal OPD for $T_{\text{eff}} = 2400K$, the second number is for $T_{\text{eff}} = 2800K$ and the third one is for $T_{\text{eff}} = 3100K$. OPD is in the unit of mm. OPD ranging from 10mm to 41mm is considered in calculation.

Table 2: Power Law Index χ as a function of Spectral Resolution R for DFDI and DE ($T_{\text{eff}} = 2400K$)

DFDI					DE		
$V \sin i$ [km · s ⁻¹]	R	5,000-20,000	20,000-50,000	50,000-150,000	5,000-20,000	20,000-50,000	50,000-150,000
0	χ	0.62	0.59	0.31	1.08	0.93	0.44
2		0.63	0.56	0.27	1.07	0.89	0.38
5		0.62	0.45	0.16	1.01	0.69	0.21
10		0.58	0.28	0.09	0.87	0.39	0.10

Table 3. Spectral Resolution and wavelength coverage on a given detector

R	$\Delta\lambda$ (nm)	$\lambda_{min} - \lambda_{max}$ (nm)
25,000	480	800–1280
30,000	400	800–1200
40,000	300	850–1150
50,000	240	880–1120
60,000	200	900–1110
70,000	170	910–1080
80,000	150	920–1070

Table 4: Q'' comparison of DFDI and DE as a function of $V \sin i$

		DFDI		DE		
	$V \sin i$ [$\text{km} \cdot \text{s}^{-1}$]	R_{optimal}	Q''_{DFDI}	R_{optimal}	Q''_{DE}	$Q''_{\text{DFDI}}/Q''_{\text{DE}}$
$\alpha=0.5$	0	50,000	7502	110,000	6623	1.065
	2	50,000	6806	75,000	6001	1.134
	5	25,000	4979	50,000	4424	1.125
	10	15,000	3394	25,000	2996	1.133
$\alpha=1.0$	0	5,000	26384	30,000	8705	3.031
	2	5,000	24297	25,000	8490	2.862
	5	5,000	18929	15,000	7884	2.401
	10	5,000	12877	10,000	7239	1.779

Table 5. Predicted IRET Performance

Name	m_J	T_{eff} (K)	$V \sin i^a$ ($\text{km} \cdot \text{s}^{-1}$)	K ($\text{m} \cdot \text{s}^{-1}$)	$\delta v_{rms,S}^b$ ($\text{m} \cdot \text{s}^{-1}$)	K_{HZ}^c ($\text{m} \cdot \text{s}^{-1}$)
GJ 1214 b ¹	9.75	3000	2	12	2.4	1.0
GJ 176 b ²	6.46	3500	1	4.1	0.58	0.57
GJ 179 b ³	7.81	3400	1	26	1.05	0.66
GJ 436 b ⁴	6.9	3684 ^d	1	18.7	0.71	0.59
HIP 57050 b ⁵	7.61	3190	1	38	0.91	0.68
GJ 649 b ⁶	6.45	3700 ^d	1	12	0.58	0.54

Note. — a: $V \sin i$ is assumed to be $1 \text{ km} \cdot \text{s}^{-1}$ if otherwise specified in references; b: the fundamental photon-limited RV uncertainty; c: velocity semi-amplitude if there is a habitable Earth-like planet locating at 0.05 AU from a host star; d: we assume T_{eff} to be 3500K because we do not have synthetic stellar spectrum with T_{eff} higher than 3500K.

References. — 1, Charbonneau et al. (2009); 2, Forveille et al. (2009); 3, Howard et al. (2010); 4, Butler et al. (2004); 5, Haghighipour et al. (2010); 6, Johnson et al. (2010)

Table 6. Mid-Late M Dwarfs Available for IRET^a

m_J	Number of Targets ^b
J≤6	25
J≤7	97
J≤8	270
J≤9	868
J≤10	2458
J≤11	6267
J≤12	12775

Note. — a: LSPM Catalog (Lépine & Shara 2005); b: we apply both color cut ($V-J \geq 3$) and m_J cut.